UNIVERSITY OF CALIFORNIA
Los Angeles

Minimizing hydraulic losses in additively-manufactured swirl coaxial rocket injectors via analysis-driven design methods

A thesis submitted in partial satisfaction
of the requirements for the degree
Master of Science in Aerospace Engineering

by

David Morrow

2020

ABSTRACT OF THE THESIS

Minimizing hydraulic losses in additively-manufactured swirl coaxial rocket injectors via analysis-driven design methods

by

David Morrow
Master of Science in Aerospace Engineering
University of California, Los Angeles, 2020
Professor Raymond M. Spearrin, Chair

Additive manufacturing (AM) has matured significantly over the past decade and become a highly attractive tool for reducing manufacturing complexity and removing traditional design constraints. This is particularly desirable for rocket combustion devices which often feature hundreds of individual parts with precise tolerances. The degree to which AM can be used to improve combustion device performance, however, has been less rigorously explored. In this work, hydraulic performance impacts associated with and enabled by AM are assessed for a liquid bi-propellant swirl coaxial injector. Specifically, a single-element liquid oxygen/kerosene injector based on a canonical design was manufactured from inconel using Direct Metal Laser Sintering at two different coaxial recess depths. Cold-flow testing for the as-manufactured baseline injector found a reduction in the designed discharge coefficients, which is primarily attributed to increased surface roughness inherent in the AM process. Quantifying this difference provides data for tuning surface roughness effects in Computational Fluid Dynamics (CFD) models, which may be used to inform the design stage. In addition, CFD simulations were leveraged to identify hydraulic losses in the baseline design and redesign a more hydraulically efficient injector geometry utilizing reductions in dramatic flow constrictions. For the modified injector geometry, computational results predict a 19% and 8% increase in the fuel and oxidizer discharge coefficients, respectively, as well as an

18% increase in angular momentum relative to the baseline. These results in addition to recommendations made for minimizing frictional losses that resulted from the printing process demonstrate how AM and analysis-driven design may be utilized to develop a more hydraulically efficient liquid rocket engine injector, thus highlighting a pathway to higher thrust-to-weight ratio propulsion systems and increased launch vehicle payload capacity. This work was presented in part at the 2019 AIAA Propulsion and Energy Conference.

The thesis of David Morrow is approved.

Jeffrey D. Eldredge

Ann R. Karagozian

Raymond M. Spearrin, Committee Chair

University of California, Los Angeles

2020

To my mother and sister

Table of Contents

List of Figures

List of Tables

List of Symbols

Symbols

A	geometric constant, or area
C_1	$k-\epsilon$ source constraint
$C_{1\epsilon}$	$k-\epsilon$ model constant
C_2	$k-\epsilon$ model constant
$C_{3\epsilon}$	$k-\epsilon$ model constant
C_D	discharge coefficient
ΔP	pressure drop
g	gravity
G_b	generation of k from buoyancy
G_k	generation of k from mean ∇V
H	head
h	film thickness
J	cell direction vector matrix
k	turbulent kinetic energy
L	recess depth
$L2$	internal impingement length
$\dot{m}$	mass flow rate
n	number of inlets

O/F oxidizer to fuel ratio

P pressure

Q volumetric flow rate

R, r radius

r_i direction vector in i^{th} direction

S source term, or cell width

U, u velocity

V velocity, or volume

V_θ tangential velocity

V_z axial velocity

Y_M fluctuating dilatation

Greek Letters

α half spray angle

ϵ dissipation rate

Γ diffusion coefficient

μ dynamic viscosity

ν kinematic viscosity

ϕ passage fullness coefficient, or arbitrary scalar

ρ density

σ turbulent Prandtl number

τ shear stress

Subscripts

ax axial

b body

c vortex core

f fuel, or cell face

i arbitrary index

in inlet

inv inviscid

k source

N nozzle

ox oxidizer

s swirl

t tangential, or turbulent

tot total

vis viscous

Superscripts

o initial

$'$ fluctuating

Acknowledgments

It is a privilege to recognize the many individuals who have made this work possible. I would first like to express my sincere gratitude to my research advisor Professor Mitchell Spearrin for his guidance and dedication to my development. Professor Spearrin inspires ambition, critical thinking, and passion, which has enabled me to grow significantly as an engineer. I would also like to thank Professor Ann Karagozian and Professor Jeff Eldredge for serving on my thesis committee and their instruction during my time at UCLA.

I would next like to thank my peers and mentors in the Laser Spectroscopy and Gas Dynamics Laboratory. It has been a privilege working along side this incredible group of people, who have been a constant source of support and encouragement. I will always cherish the many memories we have made both in and out of the lab.

Furthermore, I would like to thank Ben Tan for assistance with the resources that enabled this work. I also want to thank Dr. Brian Anderson for his invaluable advice and assistance with the CFD modeling, which he generously provided in his free time.

To conduct the more demanding CFD simulations, this work used the Extreme Science and Engineering Discovery Environment (XSEDE), and specifically the Bridges machine at the Pittsburgh Supercomputing Center. I am also highly appreciative of the Science, Mathematics, and Research for Transformation (SMART) Scholarship Program for funding this work.

Lastly, I want to recognize the many individuals in my personal life who have enabled this accomplishment. My mother has always put my needs above her own and worked tirelessly to support my goals. I would not be where I am today without her dedication. I would also like to thank my sister Katrina for continuously inspiring me to be the best I can be. Next, I would like to thank Paul and Melanie Lavery for encouraging me to attend UCLA. Finally, I am forever grateful to my loving girlfriend Sydney, who has supported me at every step of this pursuit and been the best partner I could ask for.

CHAPTER 1

Introduction

Chemical propulsion based launch vehicles are the primary means of reaching space and this is expected to remain the case for the foreseeable future. Significant engineering efforts are put into maximizing the payload mass, and thereby minimizing the payload unit cost, that a launch vehicle can deliver to orbit. Much of this effort is specifically spent on optimizing propulsion system efficiency as propellants typically comprise the largest mass fraction of overall launch vehicle mass. In liquid rocket engines, the propellant injector has one of the greatest impacts on propulsion performance and efficiency [1, 2].

The role of a liquid rocket injector is to deliver propellants to the combustion chamber and promote rapid mixing while isolating the combustion chamber dynamics from the upstream feed system. The degree and homogeneity of propellant mixing is critical to achieving complete combustion and converting the maximum amount of chemical energy into thermal energy. Furthermore, liquid atomization and vaporization are the primary drivers of the combustion chamber length, thus directly impacting overall engine weight. The injector must also maintain a sufficient pressure drop to drive the propellants into the chamber and to create stiffness against dynamic pressure fluctuations within the chamber. The pressure drop cannot be excessively high, however, as this will increase structural requirements of the upstream feed system, and thus, overall system weight. High injector pressure drop also adversely affects throttling capability, which has become increasingly important with the development of reusable launch vehicles.

In liquid rocket engines, common injector configurations include impinging, coaxial, and pintle [3]. Examples of these may be seen in Figure 1.1. The strengths and limitations of

these injector types are discussed later. In brief, the early U.S. space program relied primarily on impinging injector schemes due to their manufacturing simplicity and dependable performance. Coaxial configurations, however, offer enhanced mixing characteristics and are less sensitive to manufacturing errors. As a result, these have become the modern standard for high performing injectors. Within the coaxial category, it can be argued that swirl coaxial injectors offer the best mixing and atomization characteristics due to generation of both axial and tangential shear between the propellants streams. This leads to decreased combustion chamber length and higher engine thrust-to-weight ratio.

The increased performance of coaxial injectors comes at the cost of more significant design, analysis, and manufacturing effort. Liquid rocket injectors generally contain dozens of individual elements to enhance mixing. For coaxial injectors, each element typically consists of two or three individual parts that are joined together. These elements must then be joined to a faceplate, propellant manifolds, baffles, and a structural housing to form a complete injector assembly. At the launch vehicle scale, the overall injector assembly can consists of hundreds of individual parts, each with its own fabrication and quality inspection process. Reliability also decreases as more joints are added, since this introduces more failure points. In summary, liquid rocket injector fabrication is a highly intensive process with long manufacturing schedules and high production costs.

Fortunately, additive manufacturing (AM), also known as 3D-printing, has matured significantly over the past decade and can greatly reduce conventional manufacturing complexity, impacting both time and cost of production. In addition, AM allows engineers to re-imagine traditional designs by removing manufacturing constraints. AM encompasses a variety of methods, techniques, and materials. In particular, granular binding methods allow a variety of metals to be printed with mechanical properties and precision comparable to traditional forging and manufacturing.

In industry, AM is now being utilized at almost every major aerospace manufacturer in the U.S. [4], and AM is playing a large role in revolutionizing launch vehicle design and manufacturing. For example, the New Zealand-American company Rocket Lab manufactur-

ers all major components of their 3500-lbf Liquid Oxygen (LOx)/Kerosene engine with AM, which can be printed in its entirety in 24 hours [5]. This directly enables their mission to provide high frequency launch operations and they have successfully delivered 48 satellites to Low Earth Orbit to date. Another emerging company, Relatively Space, is trying to additively manufacture more than 90% of their launch vehicle Terran 1 [6]. By removing dependency on fixed tooling, Relativity claims to be able to manufacture an entire launch vehicle from raw materials in less than 60 days, enabling them to quickly adapt to dynamic market needs. Several university rocket projects have also successfully fabricated and tested AM liquid rocket engines, underscoring the increased accessibility of AM [7, 8].

While AM has demonstrated the ability to reduce costs and production time, the degree to which AM can be used to improve and control the fluid dynamics of combustion devices has been less rigorously explored. AM provides new opportunities to re-imagine traditional fluid devices which often feature sharp area changes and angles due to manufacturing constraints. More gradual flow branching and turning can theoretically lead to reduced hydraulic losses and more total pressure available for generating fluid momentum, resulting to enhanced mixing and shorter droplet breakup lengths. According to Hutt [9], 85% of the oxidizer pressure drop in the Space Shuttle Main Engines was lost to viscous effects, equating to an additional 1000 horsepower required by the oxidizer pump. An important consequence of the AM printing process, however, is rougher surface finish, which can increase frictional losses and counteract the potential benefits of AM-enabled geometries. Therefore, quantitative assessment of these competing factors is required.

The goal of this study is to assess and improve the hydraulic performance of an additively manufactured single-element swirl coaxial rocket injector. An analysis-driven design approach is taken by leveraging Computational Fluid Dynamics (CFD) to inform design modifications targeted at reducing hydraulic losses and increasing outlet momentum characteristics. Cold-flow testing of actual manufactured hardware is conducted and serves three purposes: (1) to validate the CFD model, (2) obtain as-manufactured hydraulic data, and (3) prepare for hot-fire testing. Chapter 1 so far has discussed this work's motivation. Next,

a review of current liquid rocket injector and AM technologies will be presented. Chapter 2 will discuss the additively manufactured injector designed and developed in this study. Chapter 3 will present the computational approach used to assess injector hydraulic characteristics. Results from CFD modeling, cold flow testing, and design modifications will be discussed in Chapter 4. Finally in Chapter 5, conclusions for this study and future directions will be presented.

1.1 Review of Liquid Rocket Injectors

The early U.S. space program relied primarily on impinging injector schemes due to their manufacturing simplicity, extensive design guidelines, and dependable performance [10]. Impinging injectors work on the principle of colliding numerous small fluid jets into one another to achieve atomization and mixing. There exists many different impinging configurations, which are categorized by the number for fluid jets and similarity of propellant. For example, an unlike doublet would be two impinging streams of fuel and oxidizer. An example of a an unlike triplet may be seen in Figure 1.1. Notable launch vehicles that utilized impinging injectors include Saturn, Titan, and early Atlas series vehicles, as well as China's Long March and Europe's Ariane [3]. Important limitations of these injector types include sensitivity to manufacturing errors and sub-optimal mixing.

As manufacturing and design capabilities have improved, however, substantial effort has been placed into developing more optimal injectors. As a result of this effort, coaxial injector configurations have become the modern standard for high performance [3]. Coaxial injector elements spray the propellants as two concentric sheets that mix via shearing at the fluid interface. This is advantageous to impinging elements due to greater fluid surface contact area, which produces two added benefits: (1) enhanced shearing which leads to more rapid mixing, and (2) less sensitivity to manufacturing errors since fluid sheets are easier to intersect than jet streams. In contrast to the U.S., the Russian space program has predominantly used coaxial injector types. Examples include the Soyuz launch vehicle and RD-180 engine used in the U.S. Atlas-V rocket. Coaxial injectors were also utilized in the Space Shuttle

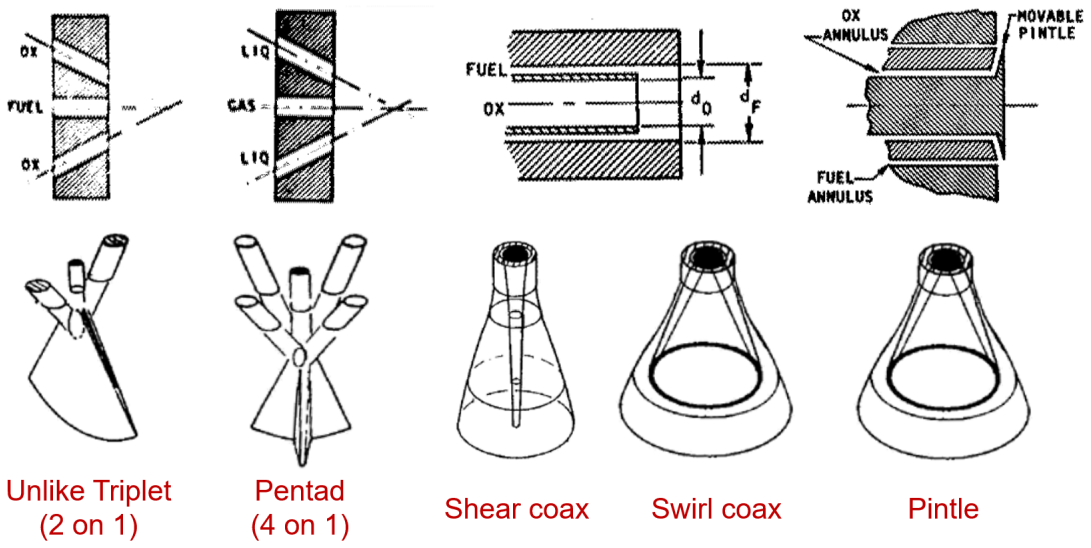

Figure 1.1: Schematic of representative liquid rocket injector types. Top row features element geometry and bottom row is corresponding fluid spray pattern. It should be noted that both the swirl coax and pintle have similar spray shapes in this depiction, but the pintle spray has no angular momentum. Reprinted from [10, 11] with permission of the American Institute of Aeronautics and Astronautics, Inc.

Main Engine.

Within coaxial injector configurations, there exists shear, swirl, and pintle element types. In shear element types, the fluid momentum and shearing is entirely in the axial direction. Swirl elements improve upon this by imparting angular momentum to the fluid streams, and therefore, an added tangential shear component. The angular momentum causes the swirling streams to spray outward and impinge with neighboring element streams as well. Consequently, swirl coaxial injectors are able to mix and atomize the propellants at shorter axial lengths. Furthermore, shear coaxial injectors exclusively employ gas-liquid propellants as they rely on a high axial momentum difference between the fluid streams to generate sufficient mixing, which is not easily achieved if densities are on the same order of magnitude. In contrast, swirl injectors have been used for both bi-liquid and gas-liquid propellant combinations, although it is typically just the liquid stream that is swirled.

In comparison to impinging injectors, it has been found that for the same flow rate and pressure drop, the mean droplet diameter produced by swirl elements is 2.2 to 2.5 times smaller [2], leading to shorter atomization length scales. Some notable disadvantages of swirl injectors, however, include increased sensitivity to instabilities and longer transient response times. As a result, swirl coaxial elements are better candidates for launch vehicle applications as opposed to in-space propulsion, which typically requires short, transient burns. In summary, it can be argued that swirl coaxial injectors are currently the best suited for maximizing engine thrust-to-weight ratio in launch vehicle applications.

The last noteworthy liquid rocket injector type discussed here is the pintle. Pintle injectors are primarily known for their excellent throttling capability, allowing them to maintain combustion stability other a wide range of operating conditions. Notable applications include the Lunar Module Descent Engine, and more recently, SpaceX's reusable Falcon 9 rocket [12]. In the pintle injector, the momentum of the inner and outer streams are in the radial and axial direction, respectively. This causes the propellants to intersect perpendicularly and redirect at some downstream spray angle. This may be seen in Figure 1.1. Additional strengths of pintle injectors include excellent atomization and mixing characteristics, and relatively simple manufacturing [3, 13]. A major challenge with pintle injector design is a lack of published guidelines and test data [14].

Selection of the appropriate injector depends on the application and consideration of the design's strengths and limitations. The discussion presented here is by no means exhaustive, but provides important context and a summary of critical considerations. In this study, it was decided to develop a swirl coaxial injector due to their relevance to large scale launch vehicles, excellent performance, and successful test demonstrations with additive manufacturing [15].

1.2 Additive Manufacturing for Rocket Combustion Devices

Within AM, there exists many methods and technologies that may be leveraged to produce a variety of parts, from rapid prototyping with thermoplastics to high precision superalloy

metals. An understanding of the capabilities and limitations of these processes is required to correctly select the appropriate method and obtain desired device performance. AM processes can be categorized by how they feed and bind the working material. In general, the material is either fed as a filament wire through an extruder or spread as a powder across a printing bed. A summary of common AM methods is provided in Table 1.1.

Table 1.1: Summary of Additive Manufacturing processes and materials.

Type	**Technology**	**Feedstock**	**Materials**
Extrusion Deposition	Fused Deposition Modeling (FDM)	Wire	Thermoplastics, some metals, ceramics
	Robocasting	Filament	Ceramics, metal alloys
Granular Binding	Selective Laser Sintering (SLS)	Powder	Thermoplastics, metals, ceramics
	Selective Laser Melting (SLM)		Titanium alloys, Stainless Steel, Aluminum
	Electron Beam Melting (EBM)		Almost any metal alloy
Photopolymerization	Stereolithography (SLA)	Liquid Resin	Photopolymers
	Digital Light Processing (DLP)		
Powder Fed	Directed Energy Deposition (DED)	Powder or wire	Almost any metal alloy

The aerospace industry has primarily utilized the SLS and SLM methods for developing combustion devices, which are capable of achieving high-tolerance precision and excellent mechanical properties for typical aerospace materials [4, 6, 15–18]. Specifically, Direct Metal Laser Sintering (DMLS), which is a subset of SLS specific to metals only, is able to achieve a density uniformity of 99.99% and is inherently preventative of internal defects. Sintering distinguishes itself from melting, as the metal is not fully liquified. The DMLS process has been chosen in this study since SLS parts have been successfully demonstrated in hot-fire testing and DMLS offers excellent part quality and precision.

A schematic of the DMLS process is shown in Figure 1.2. The DMLS process starts with a fine layer of metal powder spread over a printing bed. Typical particle diameter of the powder is on the order of tens of micrometers, which governs the powder layer height and printing speed. A laser then sinters the metal powder to create a 2D cross-section of the 3D part at the current height. After the cross-section is completed, a new layer of powder is spread on to the bed by the wiper, and then the process repeats until the part is completed.

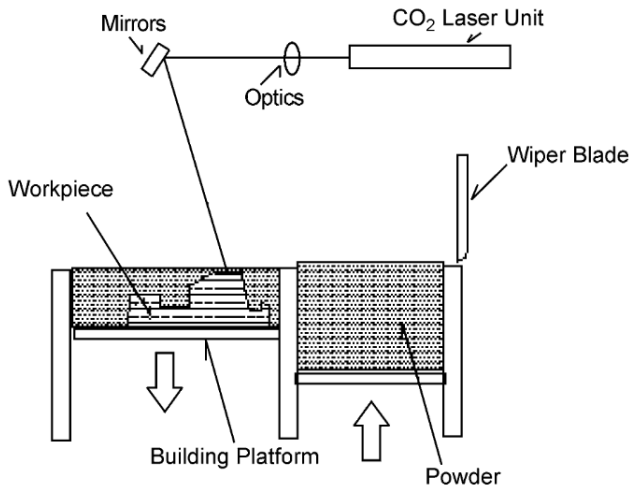

Figure 1.2: Schematic of DMSL process. Metal sintering is achieved with CO_2 or Yb-fiber lasers at power levels in the 100s to 1000s of Watts. Reprinted from [19] with permission from Elsevier.

An excellent and comprehensive demonstration of the feasibility of additively manufactured combustion devices has been published by NASA Marshall Space Flight Center (MSFC) [15]. Over the last decade, MSFC has developed combustion devices with numerous AM techniques, including SLS and SLM, and demonstrated them in hot-fire testing. This encompasses injectors, chambers, nozzles, and igniters for engines ranging in size from 100 to 35,000-lbf. Furthermore, their work has encompassed a variety of propellant combinations and injector schemes. A few notable examples may be seen in Figure 1.3 and Figure 1.4. They have found additively manufactured devices to perform comparably to their conventional counterparts in a variety of test scenarios and power levels. This provided a strong validation of AM combustion devices and supported the use of AM in the present study.

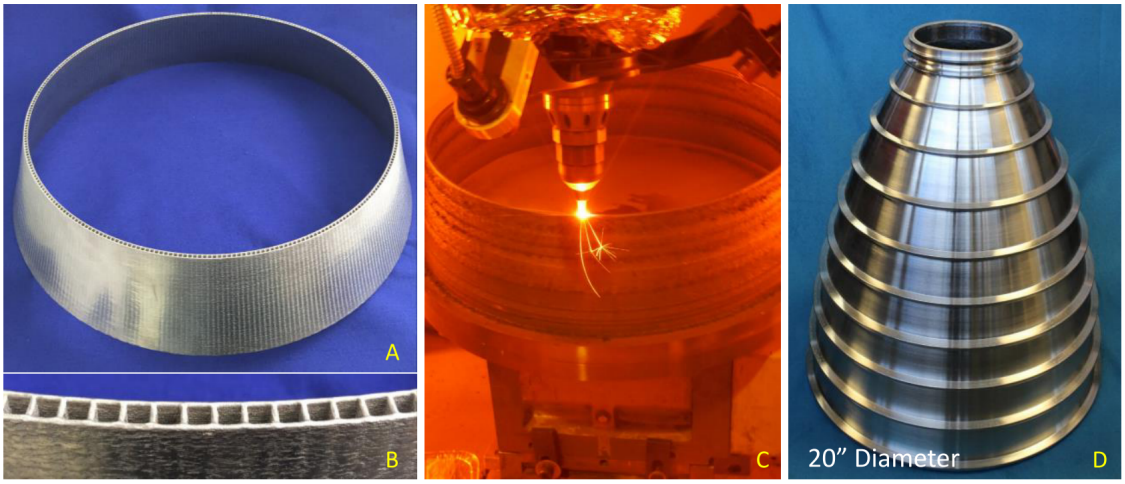

Figure 1.3: Rocket nozzle being additively manufactured at MSFC: (A) partially fabricated nozzle with cooling channels, (B) close up of cooling channels, (C) nozzle during printing, and (D) nozzle jacket after post-print polishing. Borrowed from [15].

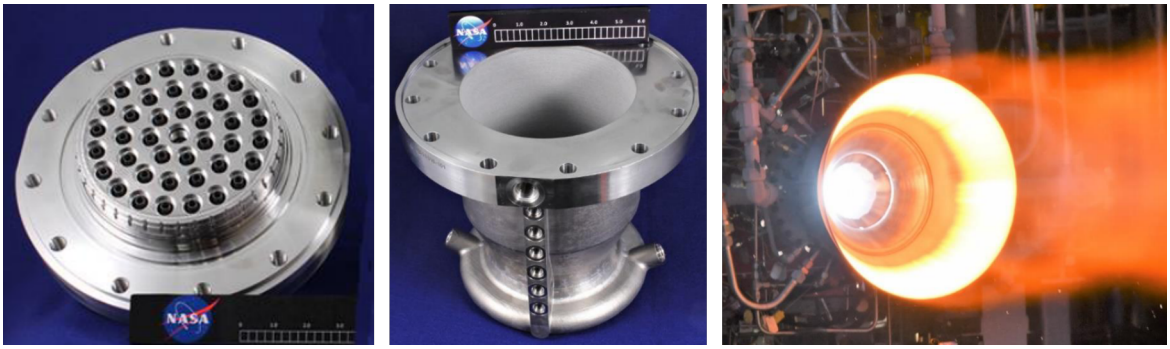

Figure 1.4: Examples of AM combustion devices developed at MSFC. From left to right: 4000-lbf swirl coaxial injector made from inconel 625, LOx/Methane engine throat made from inconel, and hot-fire test of bi-metallic nozzle extension. Borrowed from [15].

CHAPTER 2

Injector Design and Development

2.1 Swirl Coaxial Injector Design Theory

The design theory for swirl injectors in rocket applications was pioneered by Vladimir Bazarov may be found in [2]. It is based on the fundamental work describing swirling flow dynamics by Abramovich [20]. A representative single swirl element is shown in Figure 2.1. The defining characteristic is that the swirl momentum is generated by driving the fluid through inlets that are tangential to the inner swirl chamber. As a result of the swirling momentum, the fluid forms a circumferential film with a hollow gas core, which is a widely-observed phenomenon [21]. The size of the gas core and the liquid film is a function of the angular momentum and approximately independent of the flow rate. Upon reaching the nozzle exit, the swirling stream sprays outward in a conical sheet that atomizes.

Although the design methodology for swirl coaxial injectors is provided in [2], there is a clearer derivation of the governing relationships in [22]. A summary of this derivation is provided here but closely follows the notation in [2] with a few exceptions taken for clarity. The goal of this analysis is to manipulate the governing laws of fluid dynamics to a practical form that connects the desired hydraulic characteristics to the injector dimensions. The following derivation assumes steady, incompressible flow. Viscous losses and radial momentum are assumed to be negligible. In cylindrical coordinates, Bernoulli's equation states at any point along a streamline in the injector

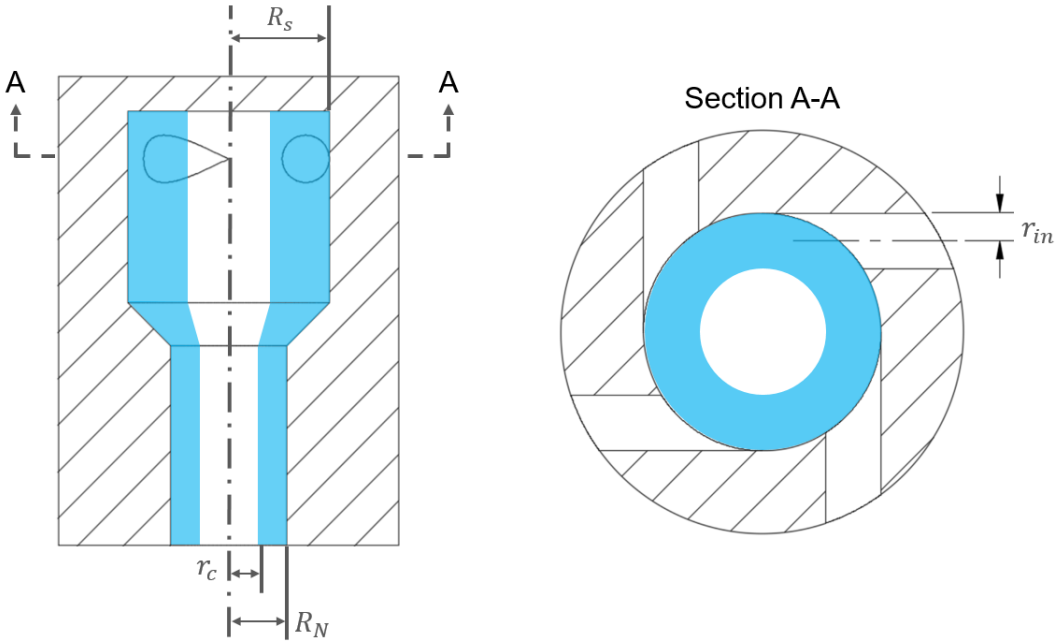

Figure 2.1: A representative swirl injector element for a single fluid.

$$\frac{P}{\rho g} + \frac{V_\theta^2 + V_z^2}{2g} = H \tag{2.1}$$

Another important relation from Bernoulli's equation may also be introduced. For any orifice type, the mass flow rate may be expressed as

$$\dot{m} = C_D A \sqrt{2\rho \Delta P} \tag{2.2}$$

By rearrangement of Equation 2.2, it can be seen that discharge coefficient is the ratio of actual to theoretical mass flow rate. For inviscid flows this value would be unity, but in real flows, this value is inversely proportional to hydraulic losses. Therefore, the discharge coefficient is a direct indicator of hydraulic efficiency and will be used extensively in this work.

Angular momentum in the fluid stream is generated by the tangential inlets. Therefore, at

any point downstream, the conservation of angular momentum yields

$$V_{\theta,in} R_s = V_{\theta,i} r_i \tag{2.3}$$

From continuity, a relation between the volumetric flow rate at the nozzle exit and the tangential inlets may be expressed as

$$Q = \pi(R_N^2 - r_c^2) V_{z,N} = n C_{D,in} \pi r_{in}^2 V_{\theta,in} \tag{2.4}$$

Where it is important to recognize that in the above equation only a portion of the nozzle exit area contains liquid as shown in Figure 2.1.

Equation 2.3 may then be substituted into Equation 2.1 for V_θ to obtain

$$\frac{P}{\rho g} + \frac{V_{\theta,in}^2 R_s^2}{2gr^2} + \frac{V_z^2}{2g} = \frac{\Delta P}{\rho g} \tag{2.5}$$

where $\Delta P = P_{feed} - P_{chamber}$. The derivative is then taken with respect to r to obtain the differential form

$$\frac{dP}{dr} = \frac{\rho V_{\theta,in}^2 R_s^2}{r^3} \tag{2.6}$$

Pressure along the swirling flow may then be found by taking the integral

$$P = -\frac{\rho V_{\theta,in}^2 R_s^2}{2r^2} + C \tag{2.7}$$

The constant is then found by applying the boundary condition at $r = r_c$, where the fluid pressure is equal to the back pressure of the gas, e.g. $P = 0$

$$C = \frac{\rho V_{\theta,in}^2 R_s^2}{2r_c^2} \tag{2.8}$$

Pressure at the nozzle ($r = R_N$) may then be written as

$$P = \frac{\rho V_{\theta,in}^2 R_s^2}{2}\left(\frac{1}{r_c^2} - \frac{1}{R_N^2}\right) \tag{2.9}$$

and using Equation 2.3 the tangential velocity is

$$V_{\theta,N} = \frac{V_{\theta,in} R_s}{R_N} \tag{2.10}$$

Where $V_{\theta,in}$ may be written in terms of the volumetric flow rate using Equation 2.4. After substitution into Equation 2.10, tangential velocity becomes

$$V_{\theta,N} = \frac{Q R_s}{n C_{D,in} \pi r_{in}^2 R_N} \tag{2.11}$$

Next, axial velocity at the nozzle exit is found by rearranging Equation 2.4

$$V_{z,N} = \frac{Q}{pi(R_N^2 - r_c^2)} \tag{2.12}$$

In addition, Bernoulli's equation at the nozzle exit gives

$$\frac{P}{\rho g} + \frac{V_{\theta,N}^2 + V_{z,N}^2}{2g} = H \tag{2.13}$$

Then by substituting Equations 2.9, 2.11, and 2.12 for P, $V_{\theta,N}$, and $V_{z,N}$, respectively, into Equation 2.13

$$\frac{Q^2}{2g\pi^2 R_N^2}\left[\frac{R_s^2 R_N^2}{n^2 C_D^2 r_{in}^4}\left(\frac{1}{r_c^2} - \frac{1}{R_N^2}\right) + \frac{r_c^4}{(R_N^2 - r_c^2)^2} + \frac{R_s^2 R_N^2}{n^2 C_D^2 r_{in}^4}\right] = H \tag{2.14}$$

The volumetric flow rate may then be found to be

$$Q = \pi R_N^2 \sqrt{2gH} \frac{1}{\sqrt{\frac{R_s^2 R_N^4}{n^2 C_D^2 r_{in}^4 r_c^2} + \frac{R_N^4}{(R_N^2 - r_c^2)^2}}} \tag{2.15}$$

This establishes the key relationship for relating the injector hydraulics to the geometry. For convenience, two non-dimensional parameters may be defined. The first is the coefficient of passage fullness

$$\phi \equiv \frac{A_{fluid}}{A_{channel}} = \frac{R_N^2 - r_c^2}{R_N^2} \tag{2.16}$$

The second parameter is the geometric characteristic constant

$$A \equiv \frac{R_s R_N}{n C_D \pi r_{in}^2} = \frac{A_N R_{in}}{A_{in} R_N} \tag{2.17}$$

where $R_{in} = R_S - r_{in}$, which locates the radial distance of the center of the tangential inlet relative to the swirl chamber. The intensity of the swirl momentum scales with this geometric ratio and is therefore often used to distinguish swirl injector designs. By substituting Equations 2.16 and 2.17 into 2.15, the volumetric flow rate may be expressed as

$$Q = \pi R_N^2 \sqrt{2gH} \frac{1}{\sqrt{\frac{A^2}{1-\phi} + \frac{1}{\phi^2}}} \tag{2.18}$$

Then taking the total velocity to be $\sqrt{2P_{tot}/\rho}$ and the maximum total volumetric flow rate to be $\pi R_N^2 \sqrt{2P_{tot}/\rho}$, the terms leftover in Equation 2.18 become the discharge coefficient

$$C_D = \frac{1}{\sqrt{\frac{A^2}{1-\phi} + \frac{1}{\phi^2}}} \tag{2.19}$$

Some additional relations may then be established to provide the designer with further insight. The non-dimensional thickness of the swirling fluid, or film, is

$$\bar{h} \equiv h/R_N = 1 - \sqrt{1-\phi} \tag{2.20}$$

The non-dimensional axial velocity in the nozzle is

$$\bar{V}_{z,N} \equiv V_{z,N}/V_{tot} = \sqrt{\frac{\phi}{2-\phi}} \tag{2.21}$$

and similarly for tangential velocity

$$\bar{V}_{\theta,N} = \sqrt{\frac{2(1-\phi)}{2-\phi}} \tag{2.22}$$

The predicted fluid half-spray spray angle is

$$tan(\alpha) = \frac{\bar{V}_{\theta,N}}{\bar{V}_{z,N}} \tag{2.23}$$

To facilitate understanding these relations may be visualized in Figure 2.2. The majority of these hydraulic parameters are shown to decrease with increasing A, or swirl intensity. The exception being tangential velocity and spray angle, which are directly proportional to angular momentum. This figure also shows as A increases, the hydraulic parameters reach a limiting value and any additional modifications to the injector geometry have a low impact.

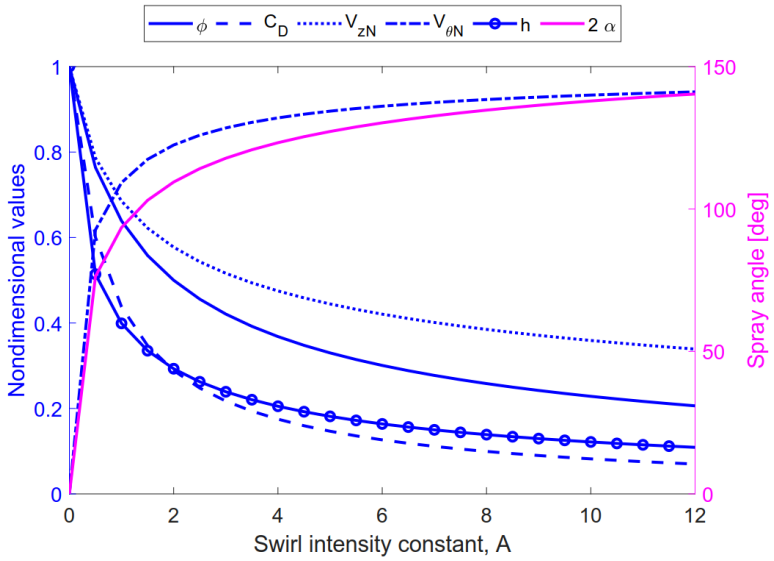

Figure 2.2: Important hydraulic parameters of swirl injector design as a function of characteristic geometric constant. Recreated from [2].

Figure 2.3 highlights two competing considerations during swirl injector design. It is desirable to increase swirl intensity, A, to enhance propellant mixing. As A increases, however, the maximum obtainable C_D decreases. This is not entirely attributed to viscous losses,

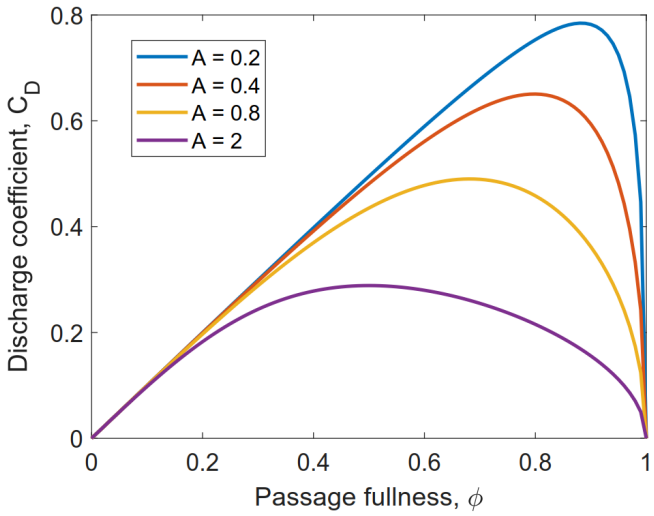

Figure 2.3: Effect of characteristic geometric constant on achievable discharge coefficient. Recreated from [2].

however. As shown in Equation 2.2, the choice of area greatly effects the value of C_D. As the angular momentum increases, the thickness of fluid film at the exit decreases, and therefore, the effective flow area and ϕ lowers. Thus reducing the C_D in a manner not associated with viscous losses.

Thus far the analysis has been general in regards to the swirl injector configuration, but several coaxial schemes exists with unique design procedures. These procedures are provided in [2] and are excluded from the current discussion. As a summary, these procedures are iterative schemes that leverage empirical data and are typically solved numerically.

2.1.1 Propellant Premixing

One of the most critical design parameters of the swirl coaxial injector configuration is the recess depth (L) of the inner post. By recessing the inner post, mixing of the propellants in the liquid phase before entering the combustion chamber is made possible. This is more generally expressed as the recess ratio (RR), which is defined as the ratio of the recess depth to the axial distance it takes the inner propellant to intersect the outer propellant. This is shown schematically in Figure 2.4. A RR less than one indicates that the propellants mix solely

in the combustion chamber, and a RR greater than one indicates that the propellants begin mixing inside the injector. The motivation to premix propellants is to increase combustion efficiency and decrease chamber length.

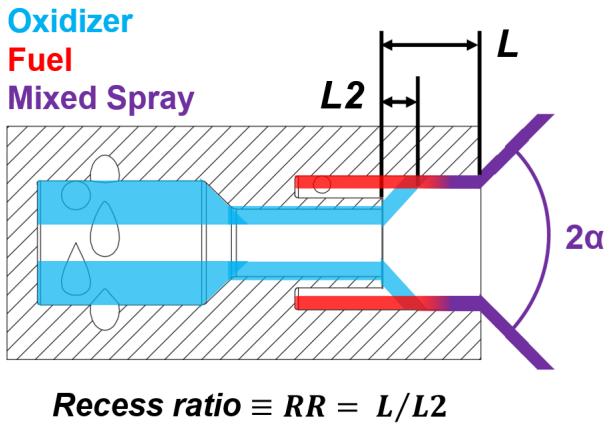

Figure 2.4: Depiction of recess ratio and intra-element propellant mixing in a representative coaxial injector. Here the inner and outer streams are oxidizer and fuel, respectively, but the opposite is also possible.

The prior analysis, however, does not provide clear guidance on how to determine the optimal recess depth. As a result, significant effort has been placed into exploring the effects of recess in non-reacting and hot-fire tests, which have characterized the impact of recess on spray characteristics, combustion efficiency, stability, and heat transfer [23–28]. It is often shown that with increasing recess, and therefore premixing, η_{C^*} approaches unity. Chamber pressure fluctuations may also increase, however, and therefore, the designed RR must be chosen carefully to obtain desired performance and stability. Kim et al. [24] found η_{C^*} to increase from 90% at RR = 0.6 to 97% at RR = 2.0 for a single-element LOx/Kerosene swirl injector while maintaining similar stability characteristics.

2.2 Design Considerations for Additive Manufacturing

Although AM offers a new design space, there are still important constraints that must be considered in order to achieve a printable part. An initial consideration is the minimum

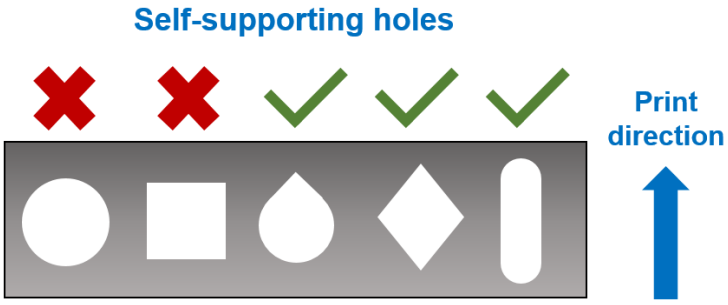

Figure 2.5: Depiction of self-supporting lateral holes. Obtaining correct geometric shape is critical to achieve designed hydraulic characteristics in additively manufactured fluid devices.

feature size and maximum build volume, which is dependent on the machine and process. For the DMLS machines leveraged in this project, minimum feature size was approximately 0.02 inch and the maximum build volume was 10x10x12 inches. The next consideration is the orientation of the part, which is related to two further constraints. First, due to the nature of building material layer by layer, perpendicular overhangs cannot be printed without support. Therefore, printing outward relative to the build direction requires the material to be gradually layered at some angle. As this angle becomes more exaggerated, the material surface finish degrades and typically cannot exceed 45° from the build direction. Second, lateral holes within the part are generally not self-supporting, and either support material must be added or the holes must take on a self-supporting cross-sectional shape as shown in Figure 2.5. Other considerations relevant to this study included post-print processes such as polishing, heat treatment, and traditional machining. Additional material considerations for AM may be found in [4].

In addition to upfront design rules, there are also part life and reliability considerations. One challenge with AM is that printed material properties are anisotropic and not easily characterized, making it difficult for the designer to assign appropriate life and reliability estimates. Internal defects within the printed part, such as micro-voids, are also difficult to detect and can lead to premature part failure. Another challenge inherent to AM is that part precision and the material deposition rate are inversely proportional, driving print time and production costs. Nondestructive testing and inspections are often used to gain

confidence in the reliability of AM parts. Fortunately, these limitations have improved with AM technology maturation and are expected to improve further with time.

2.3 Baseline Injector Design

After establishing an understanding of swirl coaxial injector design and AM methods, the next task was to decide if an injector should be developed from scratch or to leverage an existing design. The latter option was chosen so that the performance of the additively manufactured test articles could be compared to an established design as a baseline. After a review of published designs in literature, a canonical swirl coaxial injector developed by the Korea Aerospace Research Institute (KARI) was found that matched the scope of this project [24, 29]. This was a single-element injector designed for LOx/Kerosene. The KARI group has several publications detailing this injector design with extensive cold-flow and hot-fire test data [24, 29–32]. A schematic of this injector design is shown in Figure 2.6. Parameters in Table 2.1 and Figure 2.6 are consistent with the KARI design to the best of the author's knowledge, with the exception of the fuel discharge coefficient which was found to be approximately 0.045 for Kim et al. [24]. For this study, recess ratios of 0.6 and 2.0 were chosen in order to explore the effects of external and internal mixing, respectively.

From the established swirl element design, the outstanding design tasks were to modify the geometry for 3D printing using the DMLS guidelines and determine the manifold structure. Inconel 625 was chosen as the design material due to its excellent strength at high temperatures, relatively low cost with AM, and proven hot-fire performance [15]. The final injector design developed in this work may be seen in Figure 2.7 and a summary of its characteristics is provided in Table 2.2.

An important design objective was to print the injector as a single body in order to minimize sealing and isolate the propellant streams. Another goal was to minimize the part footprint. An octagon shape was chosen to accomplish this for three reasons: it provides flat surfaces for sealing fittings, it has a minimal footprint size, and it has good structural

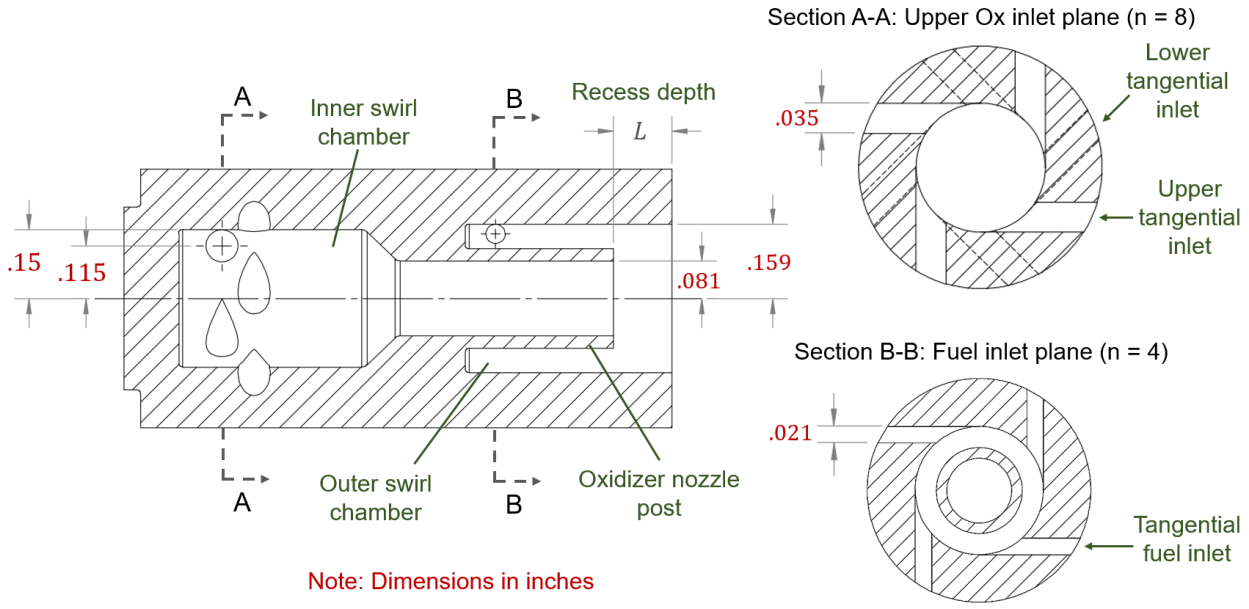

Figure 2.6: Schematic of the swirl coaxial injector design used in this study. Developed by Kim et al. [24].

Table 2.1: Analytical hydraulic characteristics of baseline injector.

Stage	A	ϕ	h (in)	$C_{D,inv}$	$C_{D,vis}$	2α (deg)
Ox	0.98	0.64	0.032	0.443	0.369	65
Fuel	13.19	0.20	0.016	0.064	0.063	120

integrity. In order to avoid finish machining near the injector exit, the injector was designed to be printed in the orientation shown on the right of Figure 2.8. To make this possible, however, support material was added underneath the oxidizer swirl chamber to suspend it during printing and had to be machined away later.

To prevent hole closure and overhang issues, the tangential inlets were given teardrop cross-sectional shapes and the propellant manifolds were angled at 45°. When adapting the circular inlets to teardrops, the cross-sectional area was kept constant. The effect of the teardrop shape on hydraulic characteristics was explored computationally (to be discussed later). To achieve proper threading for the tube fittings, the pilot holes were not printed,

Table 2.2: Summary of the baseline injector design.

Parameter	**Selection**
Number of Elements	Single
Swirl type	Co-swirling
Propellants	LOx/Kerosene
O/F MR	2.56
Recess Ratios	0.6 & 2.0
Material	Inconel 625
AM Method	DMLS
Manufacturer	i3D MFG, LLC

but instead were indicated with conical voids and were drilled and tapped afterwards. Additionally, the chamber sealing groove was undersized for printing and turned away on a lathe afterwards so that a smooth surface finish was obtained.

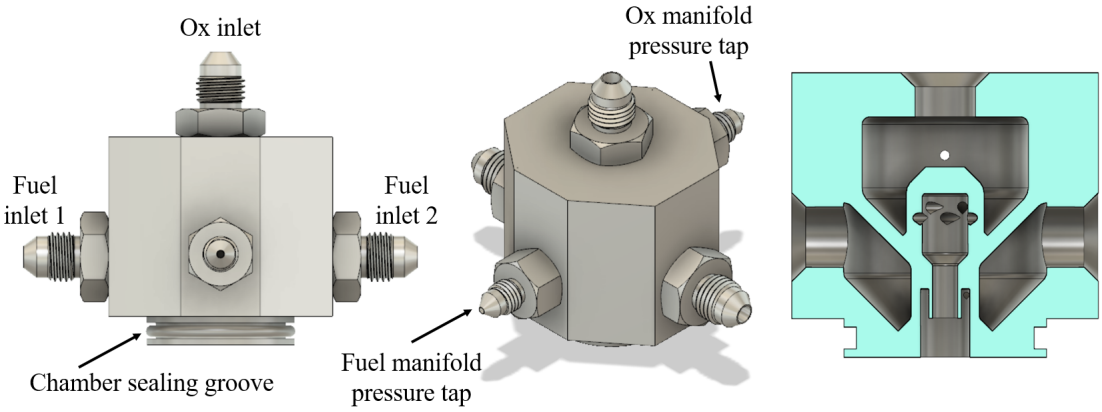

Figure 2.7: CAD model of baseline injector with front, isometric, and cross-sectional views.

Two injectors of this design were printed by i3D MFG, LLC. Both injectors were printed with the shallower recess, RR = 0.6, in order to save costs, and the oxidizer post of one injector was milled down after printing to the depth corresponding to RR = 2.0. The

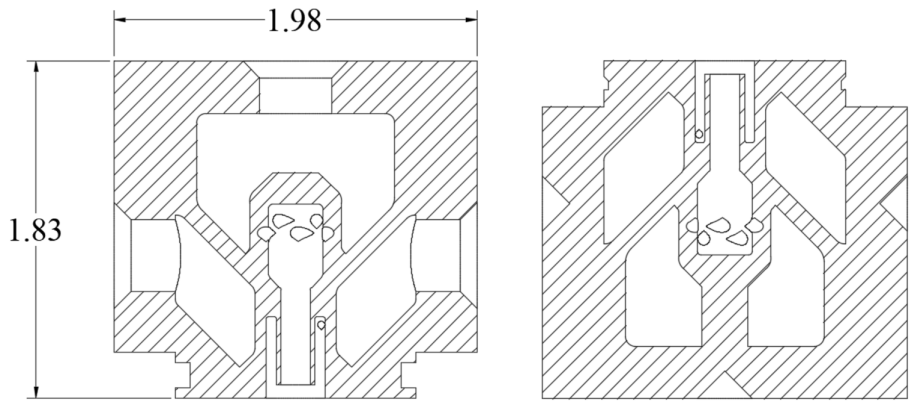

Figure 2.8: (*left*) Cross-sectional view of final desired injector with overall dimensions in inches and (*right*) Injector in printing orientation with supports.

external dimensions of both injectors after printing measured within the assigned tolerances. The finalized injectors after post-print machining operations are shown in Figure 2.9.

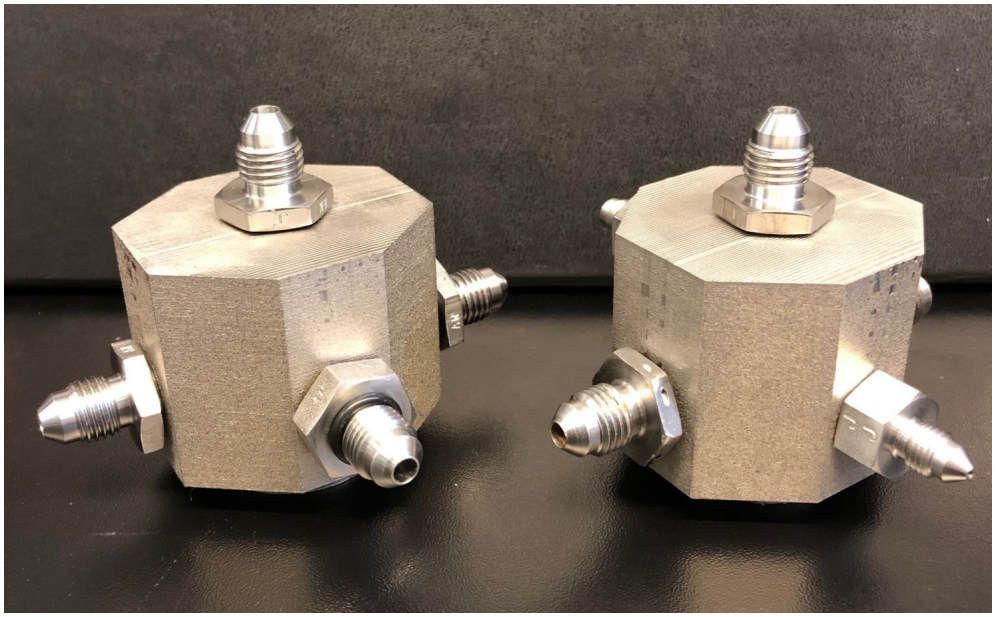

Figure 2.9: Baseline injectors after completing manufacturing.

CHAPTER 3

Computational Methods

3.1 Objectives and Approach

The goal of the CFD modeling effort was to develop an analytical tool to drive injector design and quantitatively assess hydraulic performance. Since the intention of leveraging AM was to design improved internal flow passageways, 3D simulations were conducted within the injector geometry. It was decided to use the commercial software package ANSYS Fluent, which has been demonstrated to be accurate for a variety of fluid dynamics problems, including wall-bounded viscous flows. This enabled time efficiency and substantially reduced the initial model development effort.

This approach allowed several key hydraulic metrics to be obtained, such as discharge coefficient, outlet momentum, and film thickness. These metrics provided direct evaluation of hydraulic losses and indirect indications for mixing and atomization. The numerical strategy was formulated around capturing these metrics accurately. The injector flow behavior and hydraulic characteristics were reasoned to be independent of time and therefore steady state simulations were conducted. The Reynolds-averaged Navier-Stokes (RANS) equations govern turbulent flow and the k-ϵ model was used for 1st-order closure. A notable limitation of this approach is that the boundary layer, turbulent structures, and mixing scales are not fully resolved, excluding insight into these phenomena. This information was deemed unnecessary, however, for obtaining the information needed to compare and drive initial injector designs.

Due to the formation of a hollow gas core within the swirler, a multiphase model was required to accurately capture flow behavior. Based on recommendations from the Fluent

user manual and examples in literature, the Volume of Fluid (VoF) multiphase model was chosen [33–35]. Additionally, liquid water was used to simulate the actual propellants with the understanding that the difference in density and viscosity would change mixing behavior and film thickness, but not effect discharge coefficient. A summary of the models and methods used in this study is provided in Table 3.1.

Table 3.1: Summary of models used in CFD simulations.

Category	**Model**
Discretization Method	Finite Volume
Momentum Discretization	QUICK
Pressure Interpolation	PRESTO!
Turbulence	Realizable k-ϵ
Multiphase	VoF
Wall Functions	Standard

3.2 Governing Equations

Fluid dynamics are governed by the Navier-Stokes equations - which represent the conservation of mass, momentum, and energy. For incompressible flows, the energy equation is decoupled and temperature becomes a passive scalar in the flow. The continuity equation acts as a kinetic constraint enforced by the fluid pressure. Due to the non-linearity and complex differential form of these equations, as shown in Figure 3.1, numerical methods are often employed to solve real fluid problems. This is otherwise known as Computational Fluid Dynamics (CFD). A brief description of the numerical methods used in this work within the Fluent software is presented here.

ANSYS Fluent utilizes the Finite Volume Method (FVM) for discretizing the governing fluid equations [36]. In the FVM, the physical domain is divided into numerous, discrete control volumes, or cells. Scalar flow properties are stored at the cell centroid and the fluxes

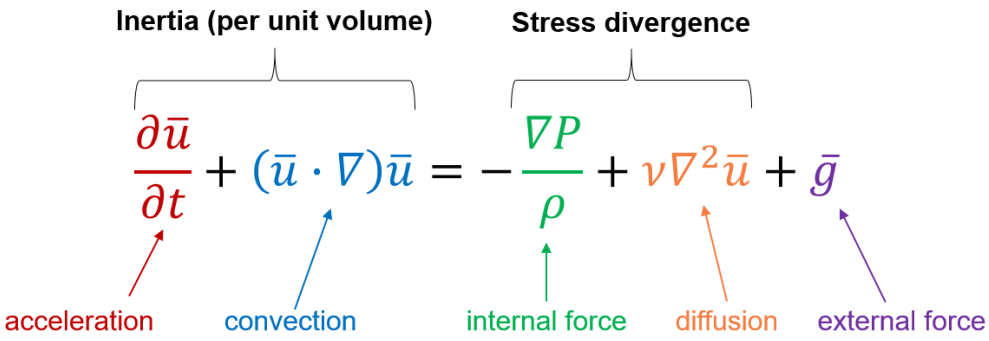

Figure 3.1: Identification of components in Navier-Stokes momentum equation for incompressible, Newtonian fluids.

between cells are stored on the faces. Since the flux entering the adjacent cell is automatically equal to the flux leaving the current cell in this framework, the FVM is conservative by nature. The FVM begins with the differential scalar transport equation

$$\frac{\partial}{\partial t}(\rho\phi) + \nabla \cdot (\rho V \phi) = \nabla \cdot \Gamma_\phi \nabla \phi + S_\phi \tag{3.1}$$

where ϕ is a scalar representing mass, momentum, energy, etc. [37]. As a simple example for the 2D rectangular grid shown in Figure 3.2, integrating this equation over the control volume ΔV for cell P produces

$$\frac{(\rho\phi)_P - (\rho\phi)_P^o}{\Delta t}\Delta V + \left(\rho u\phi - \Gamma\frac{\partial\phi}{\partial x}\right)_e A_e - \left(\rho u\phi - \Gamma\frac{\partial\phi}{\partial x}\right)_w A_w + \left(\rho u\phi - \Gamma\frac{\partial\phi}{\partial x}\right)_n A_n - \left(\rho u\phi - \Gamma\frac{\partial\phi}{\partial x}\right)_s A_s = S_\phi \Delta V \tag{3.2}$$

Equation 3.2 represents the conservation of the scalar ϕ over the control volume. Since no approximations have been made, this is still an exact equation. The manner in which the spatial and temporal gradients are disctretized depends on the specific numerical scheme

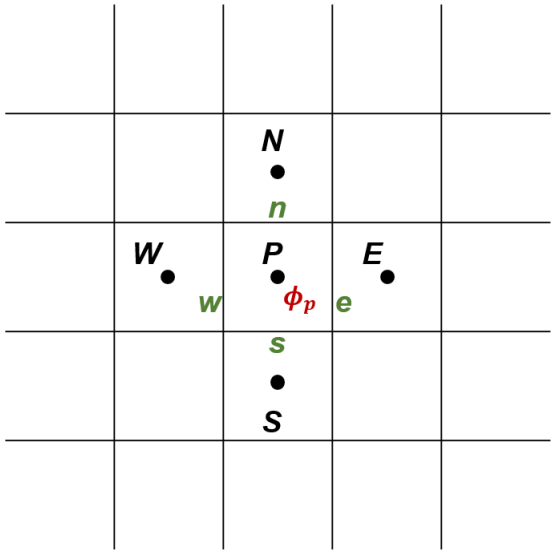

Figure 3.2: Example of uniform 2D rectangular grid with cell centroids and faces labeled.

used. Although a simple example is used here, the FVM extends to 3D space and arbitrary grids.

ANSYS Fluent has both segregated and coupled pressure-velocity algorithms for iteratively solving the discretizied equations. The coupled method was chosen in this work which significantly improves convergence but at the expense of greater memory usage. In the coupled method, the momentum equation is solved simultaneously with a pressure-based continuity equation that is updated by the mass flux at each iteration, as opposed to using typical predictor-corrector steps. For pressure interpolation, the pressure field was computed using the Pressure Staggering Option (PRESTO!) scheme, which is better suited for highly swirling flows in comparison to other interpolation methods [36].

3.3 Spatial Discretization

To numerically solve the governing equations, discretization of the spatial gradients is required. This is typically done with upwind schemes, which determine cell face variables using information from the upstream cell centroids, relative to the direction of normal velocity. The Quadratic Upstream Interpolation for Convective Kinematics (QUICK) high-order

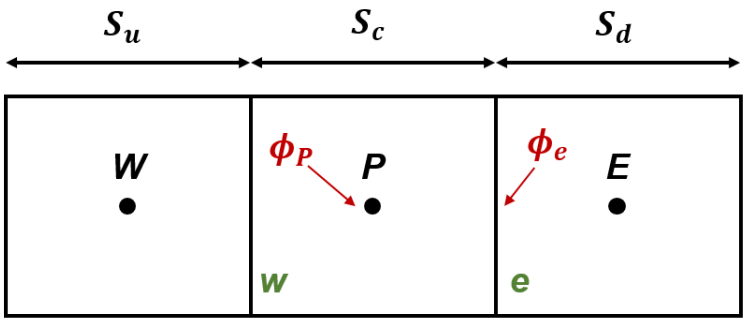

Figure 3.3: Representation of QUICK scheme for finding scalar flux on face 'e' in 1D.

scheme was used in this work due to its robust compatibility with Fluent's pressure-based solver and improved handling of swirling flows. An example using the QUICK scheme for finding a cell face flux in 1D is

$$\phi_e = \theta\left[\frac{S_d}{S_c+S_d}\phi_P + \frac{S_c}{S_c+S_d}\phi_E\right] + (1-\theta)\left[\frac{S_u+2S_c}{S_u+S_c}\phi_P - \frac{S_c}{S_u+S_c}\phi_W\right] \tag{3.3}$$

where the W, P, and E identify the cell centroids shown in Figure 3.3. In Equation 3.3, $\theta = 1/8$ for the QUICK scheme, placing more weight on the upstream face 'w'.

Gradient interpolation of the solution variables is then needed to evaluate diffusive fluxes and velocity derivatives. This was done using a least squares cell-based method. In this method, the gradient is assumed to vary linearly between neighboring cells. This can be written as

$$\nabla\phi_i \cdot r_i = (\phi_{i+1} - \phi_i) \tag{3.4}$$

After writing this equation for each neighboring cell, the following linear system of equations is obtained

$$\big[J\big]\nabla\phi_i = \Delta\phi \tag{3.5}$$

Which is over-determined and solved using the Gram-Schmidt process [38].

3.4 Viscous and Turbulent Flow Modeling

To account for turbulence, the RANS equations may be used which decompose the flow field into mean and fluctuating components. The decomposed velocity is

$$u_i = \bar{u} + u_i' \tag{3.6}$$

where $i = 1, 2, 3$ in 3D space. The RANS equations may then be written as

$$\frac{\partial \bar{u}_i}{\partial x_i} = 0 \tag{3.7}$$

$$\rho \frac{\partial \bar{u}_i}{\partial t} + \rho \bar{u}_j \frac{\partial \bar{u}_i}{\partial x_j} = -\frac{\partial \bar{p}}{\partial x_i} + \frac{\partial}{\partial x_j}\left[\bar{\tau}_{ij} - \rho \overline{u_i' u_j'}\right] \tag{3.8}$$

Where the Reynolds stresses ($\overline{u_i' u_j'}$) are unclosed. Closure is achieved by using the k-ϵ model, which provides two independent transport equations for the turbulent kinetic energy (k) and dissipation rate (ϵ). The model assumes the flow is fully turbulent, which is true for the conditions in this study. The k-ϵ model is widely popular due to is robustness, computational efficiency, and reasonable accuracy [36, 39]. It should be noted that this model is semi-empirical. In this study, the realizable version of the k-ϵ model was used, which improves upon the standard model by providing an alternative formulation of the turbulent viscosity and a modified transport equation for the dissipation rate. The realizable k-ϵ equations are

$$\frac{\partial}{\partial t}(\rho k) + \frac{\partial}{\partial x_j}(\rho k u_j) = \frac{\partial}{\partial x_j}\left[\left(\mu + \frac{\mu_t}{\sigma_k}\right)\frac{\partial k}{\partial x_j}\right] + G_k + G_b - \rho\epsilon - Y_M + S_K \tag{3.9}$$

$$\frac{\partial}{\partial t}(\rho \epsilon) + \frac{\partial}{\partial x_j}(\rho \epsilon u_j) = \frac{\partial}{\partial x_j}\left[\left(\mu + \frac{\mu_t}{\sigma_\epsilon}\right)\frac{\partial \epsilon}{\partial x_j}\right] + \rho C_1 S \epsilon - \rho C_2 \frac{\epsilon^2}{k + \sqrt{\nu\epsilon}} + C_{1\epsilon}\frac{\epsilon}{k} C_{3\epsilon} G_b + S_\epsilon \tag{3.10}$$

In turbulent flows, walls not only enforce the no-slip condition but also fundamentally change the fluid behavior, which must be accounted for with appropriate models and meshing. There are two main approaches for modeling the flow near the walls. The first is to resolve the boundary layer with a fine grid resolution, resulting in greater accuracy but increased computational expense. The second approach is to use wall functions that approximate the viscous sublayer and bridge the free stream conditions to the wall. In the realizable k-ϵ framework, it is recommended to keep near-wall spacing coarse and use wall functions. Therefore, the second approach was used with standard wall functions, which provided sufficient accuracy for this study at a reduced mesh complexity and calculation time.

3.5 Multiphase Flow Modeling

As previously mentioned, the formation of a hollow liquid core in the swirler element significantly impacts the fluid momentum within the injector. Therefore, a multiphase model was required to accurately describe the flow. After examining the available models in Fluent and looking at approaches in other studies [34, 35], it was decided to use the VoF model. The VoF model can simulate multiple immiscible fluids by solving a single set of momentum equations while tracking the fluid volume fractions at every cell. Since the VoF model is commonly used in jet breakup, this approach also served as preparation for future modeling of injector mixing and atomization. For steady state simulations, the implicit VoF equation in discrete form for the q^{th} phase is

$$\sum_{f} \left(\rho_q^{n+1} U_f^{n+1} \alpha_{q,f}^{n+1} \right) = \left[S_{\alpha,q} + \sum_{p=1}^{n} (\dot{m}_{p,q} - \dot{m}_{q,p}) \right] V \tag{3.11}$$

3.6 Unstructured Meshing and Boundary Conditions

The mesh was constructed using the ANSYS Mechanical software. Unstructured meshing techniques were used to create an initial mesh of 1.61×10^6 cells as shown in Figure 3.4. The primary effort for generating the mesh was placing appropriate local sizing controls on the tangential inlets and swirl chamber, since these regions would experience the steepest gradients. Inflation layers were placed on the injector walls as a tool to better resolve the geometry, but were kept coarse to satisfy the k-ϵ model requirements. Finer mesh sizes were explored in order to assess the independence of the numerical results.

The boundary conditions are shown in Figure 3.4 and were adapted from the test conditions reported in [24]. The domain begins upstream of the manifolds and ends at the nozzle exit. An average pressure specification was placed on the outlet boundary so that the actual flow properties were allowed to vary. Turbulent boundary conditions were set by the intensity and hydraulic diameter. The hydraulic diameter was known exactly and intensity was set to 5%, which is an educated guess for wall-bounded flows.

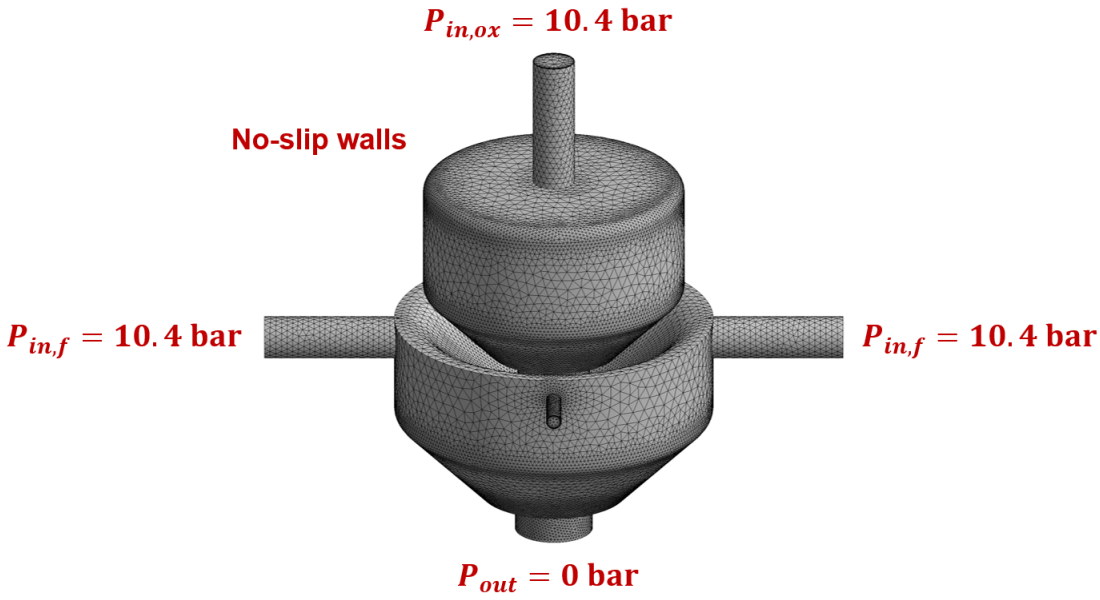

Figure 3.4: Representative unstructured 3D mesh of internal fluid domain with boundary conditions.

CHAPTER 4

Results

4.1 Mesh Refinement Study

Simulations were conducted at three different mesh resolutions in order to assess the independence and accuracy of the CFD results. The local grid sizing for the swirl element was refined between meshes since this is where the largest spatial gradients would occur. These meshes are shown in Figure 4.1. The global settings and upstream sizing controls near the inlets remained unchanged.

Discharge coefficient and net wall shear force were compared between mesh sizes and are reported in Table 4.1. The net shear force was determined within Fluent by taking the surface integral of the shear stress magnitude over the injector walls. The simulations were run until steady-state behavior was achieved. At the coarsest mesh resolution, the residuals leveled out at a magnitude of 10^{-4}. For the middle and finest mesh resolutions, the residuals leveled out at a magnitude of 10^{-5}. This provided a good indication of increased accuracy for the higher mesh resolutions.

Table 4.1: Effect of mesh resolution on global hydraulic metrics.

Mesh size (No. of cells)	$\boldsymbol{C_{D,ox}}$	$\boldsymbol{C_{D,f}}$	**Net wall shear (lbf)**
1.61×10^6	0.345	0.070	0.607
3.53×10^6	0.370	0.068	0.719
8.04×10^6	0.376	0.070	0.718
Theoretical $C_{D,vis}$	0.369	0.063	-

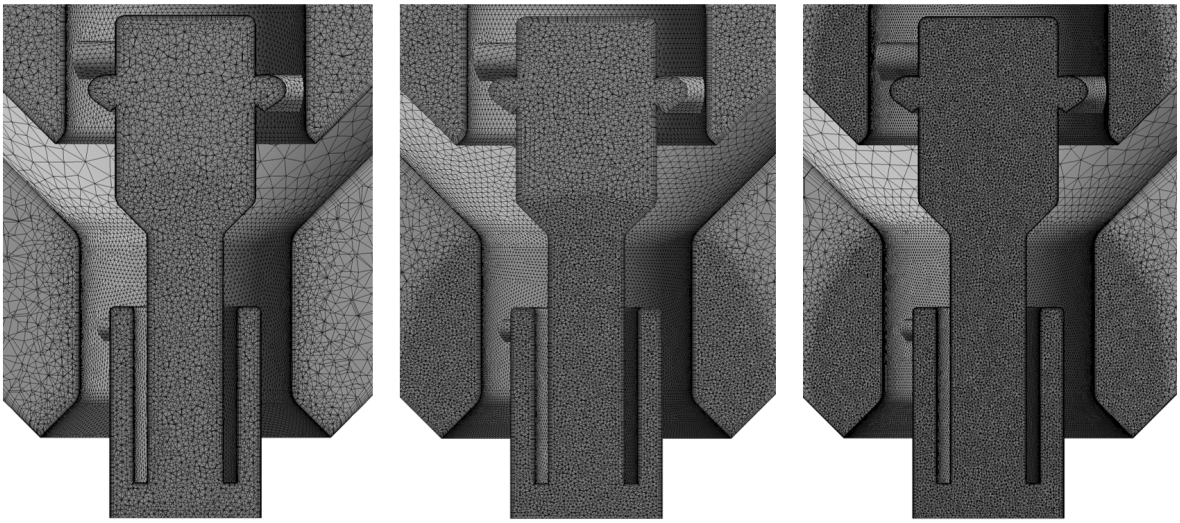

Figure 4.1: Cross-sectional view of the three mesh sizes used in this study zoomed in on swirl element.

Overall, discharge coefficient remained approximately constant with each mesh size, except for the oxidizer C_D at the coarsest mesh. The medium and fine mesh results for C_D agreed well with the theoretical prediction in Table 2.1, which has been included in Table 4.1 for convenience. This provided a good validation for the model and placed confidence in the results. The total wall shear force changed significantly from the coarse to the medium mesh, but remained consistent at the finest mesh. Since the results for the medium and fine meshes agreed well, the medium mesh size was used for remaining simulations with confidence and less computational expense.

4.2 Effect of Unconventional Fluid Passages

As mentioned previously, the cross-sectional shape of the tangential inlets was changed from a circle to a self-supporting teardrop in order to prevent lateral hole closure. It was desired to understand the effect of this change on the hydraulic characteristics before manufacturing. A literature search did not yield any definitive insight on flow in teardrop passagways, and therefore, it was decided to model injector designs utilizing both inlet geometries. Each

design was modeled using the previously discussed approach.

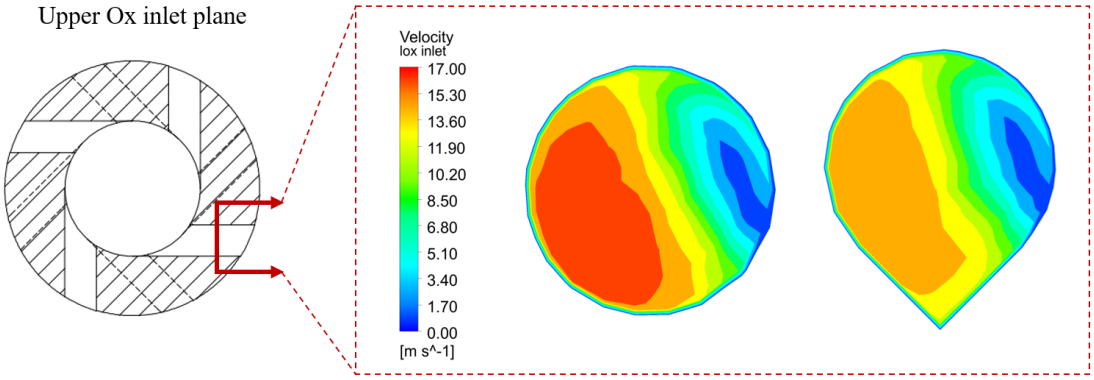

Figure 4.2: Comparison of velocity magnitude in circular and teardrop shaped channels.

As seen in Figure 4.2, the maximum velocity in the channel was found to differ, but there is similar flow separation behavior and passage fullness. Although only one set of oxidizer inlets is shown in Figure 4.2, this behavior was identical for all other tangential inlets. Most importantly, the difference in discharge coefficients between the channel shapes was less than 1.5%, and it was decided that no further design modification to the tangential inlets was required. It was at this point that the injectors were approved for manufacturing.

4.3 Model Validation with Flow Testing

Once injector manufacturing was completed, cold-flow testing was conducted in order to observe the injector spray characteristics and determine as-manufactured discharge coefficients. This served to validate the design process as well the computational results. Testing was conducted using liquid water as an inert surrogate for the propellants. The discharge coefficient was calculated using Equation 2.2. The mass flow rate was determined by timing the test and weighing the collected spray mass. The injector was discharged to atmospheric pressure, and therefore, the pressure drop was determined solely from the pressure gauge upstream of the injector. A schematic of this test setup is shown in Figure 4.3.

As reported in Table 4.2, the discharge coefficient was found to be approximately the

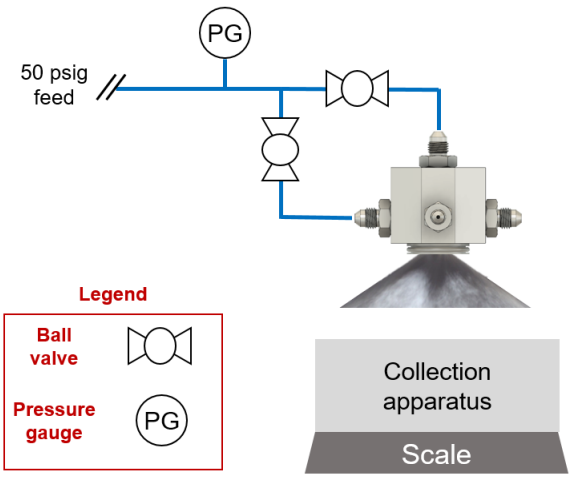

Figure 4.3: Schematic of experimental cold-flow testing.

same for both RRs as expected. The spray angles were found to agree well with the design value. At the higher RR, the oxidizer spray stream is shown to decrease as a result of internal impingement of the fluid stream with the fuel annullus wall. It is important to note that since water is being used as the working fluid, the oxidizer and fuel nomenclature is used to distinguish between the inner and outer streams, respectively. This terminology is used consistently throughout the remaining discussion.

The experimental $C_{D,ox}$ and $C_{D,f}$ were found to be 13% and 8% lower, respectively, than the theoretical prediction in Table 2.1, and 13% and 15% lower, respectively, than the computational result at the medium mesh size. This suggests that there is an added hydraulic resistance as a result of the printing process that is not captured by the models, even though they account for viscous effects. This is likely due to the increased surface roughness of the printed injector, which is not accounted for in the CFD model. With the experimental C_D now known, surface roughness parameters may be tuned in the CFD model to reach agreement and determine a relative pipe roughness. Another potential cause of the less than expected C_D is shrinkage of the tangential inlets due to material cooling during the printing process, which has been found to occur for DMLS in other studies [40]. Since the tangential inlets are inaccessible to traditional measurement devices, it is unknown whether they are within the designed tolerance. Lastly, viscous wall functions used in the CFD

Table 4.2: Cold-flow test results for baseline injector.

-	Ox		Fuel	
RR	C_D	2α	C_D	2α
0.6	0.320	63.5°	0.058	115.1°
2.0	0.290	22.7°	0.059	115.3°
Uncertainty	.012	2°	.013	2°

model only approximate the boundary layer and may also contribute to this discrepancy. In this study, the usefulness of CFD is primarily in comparing relative changes between designs. The expectation is that the computational and experimental results may differ but will trend together between injector designs.

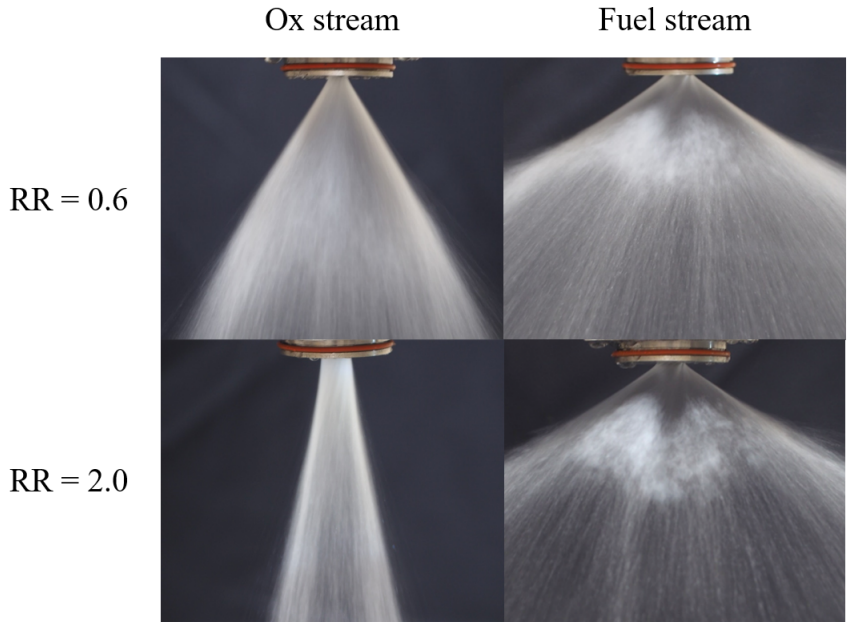

Figure 4.4: Cold-flow testing at 50 psig feed.

4.4 Results for Baseline Injector Design

Using the established CFD model at the medium mesh size, the results of the baseline injector at both recess ratios were analyzed in detail. The streamlines are shown in Figure 4.5 for flow visualization. Velocity, pressure, and shear stress contours were examined throughout the injector domain. In Figures 4.6 and 4.7, it was found that the fluid experiences a *vena contracta* effect due to the narrowness of the tangential inlets and the viscosity of the fluid. This reduces the effective flow area in the inlets and decreases their C_D. The next design iteration would focus on eliminating the *vena contracta* effect.

Another area of concern that was identified was the oxidizer nozzle tapering. As shown in Figure 4.9, the shear stresses were found to be relatively high due to the increased mass flux and 45° contraction angle in the nozzle. Reducing this peak shear stress would be another goal of the next design iteration.

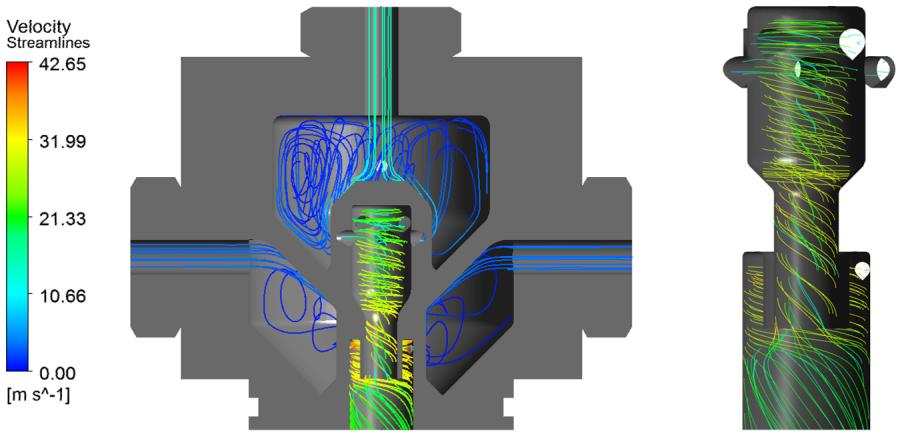

Figure 4.5: Velocity streamlines (*left*) in cross-sectional plane of baseline injector with RR = 2.0. and (*right*) zoomed in on swirl element.

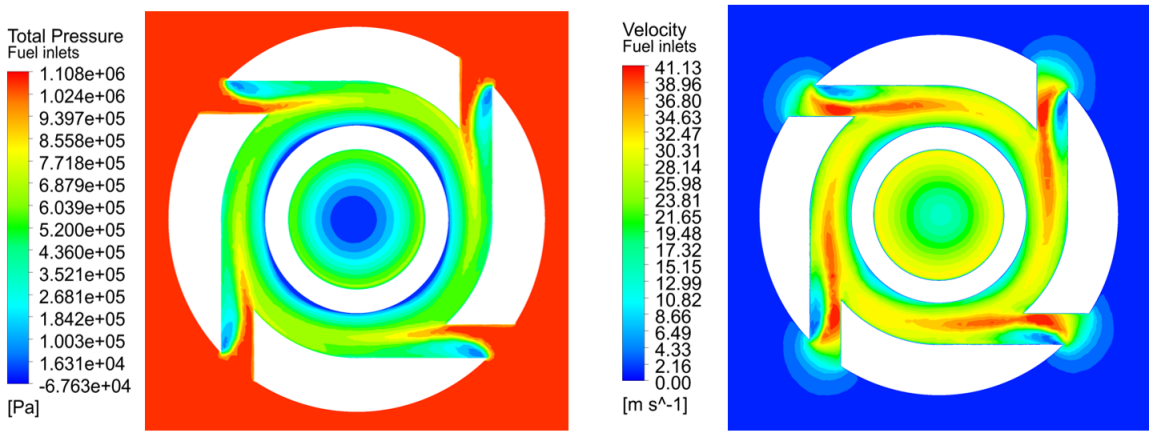

Figure 4.6: Contours at the fuel inlet plane of (*left*) total pressure and (*right*) velocity magnitude.

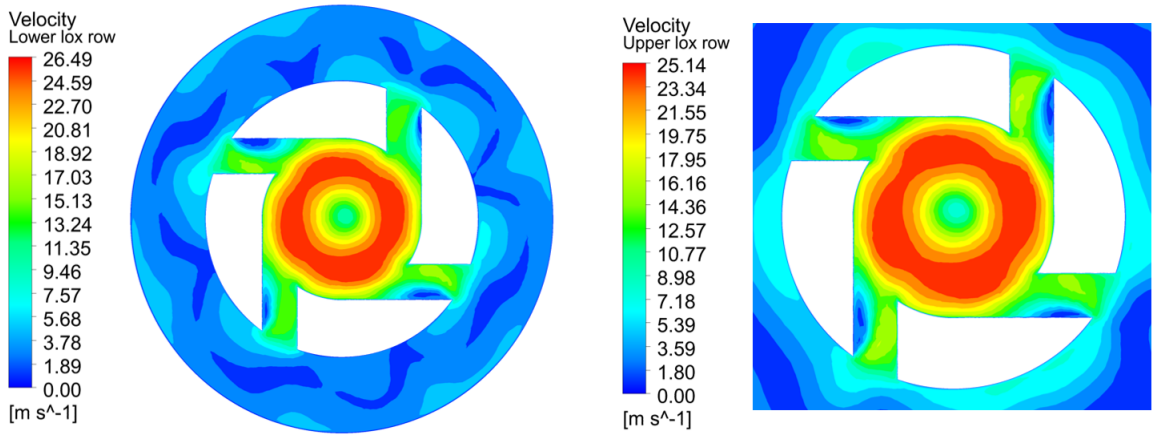

Figure 4.7: Contours of velocity magnitude at the (*left*) lower ox inlet plane and (*right*) upper ox inlet plane.

4.5 CFD-driven Design Methodology

In order to prevent the inlet separation in Figures 4.6 and 4.7, the tangential inlets were given a 20° taper and sharp edges were given fillets, as shown in Figure 4.8. By reducing the *vena contracta* effect in the inlets, the effective flow area was anticipated to increase and drive ϕ towards unity. Similarly, Figure 4.9 graphically depicts the redesign process aimed at reducing shear stress in the oxidizer nozzle. The nozzle contraction angle was reduced from 45° to 35° and larger fillets were added to the nozzle edges to make the constriction more

gradual. Both design modifications were anticipated to increase C_D and outlet momentum via reducing both form and viscous losses. These metrics would be compared between the designs in order to quantify the effectiveness of these changes.

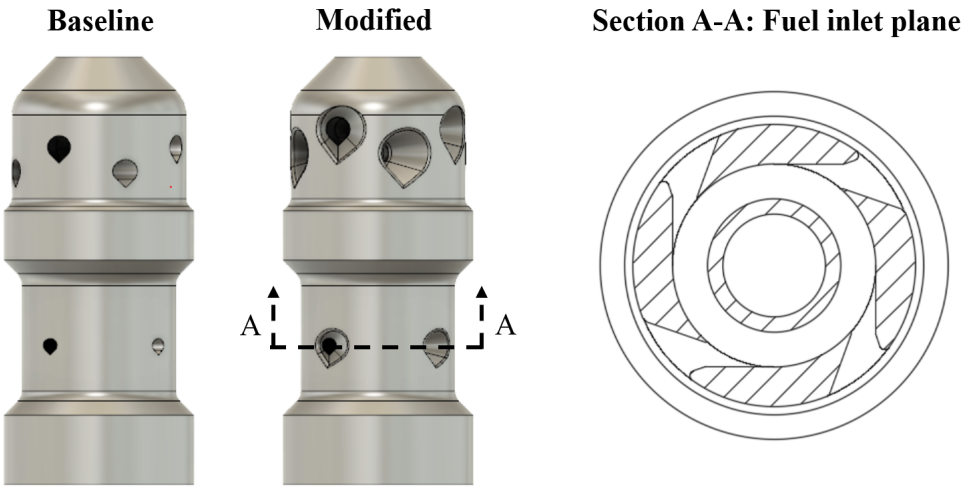

Figure 4.8: Depiction of tapered tangential inlets for modified design.

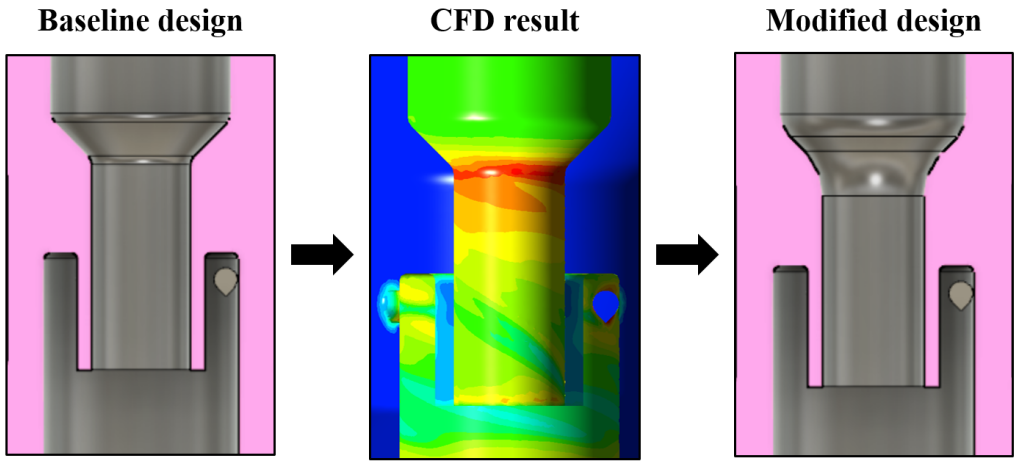

Figure 4.9: Depiction of CFD-driven redesign for oxidizer post nozzle. Contours depict relative wall shear stress magnitude.

4.6 Results for Modified Injector Design

The modified injector was modeled in an identical fashion to the baseline design. All mesh, solver, and boundary settings were unchanged. Since the geometry was altered, the exact mesh size consisted of 3.64×10^6 cells, which varied slightly from the baseline but is considered to have a negligible effect on the results. Figures 4.11 and 4.10 provide a direct comparison between the injector designs. There is a clear decrease in wall shear stress and increase in fluid momentum in both the oxidizer post and tangential inlets as a result of the more gradual fluid constrictions.

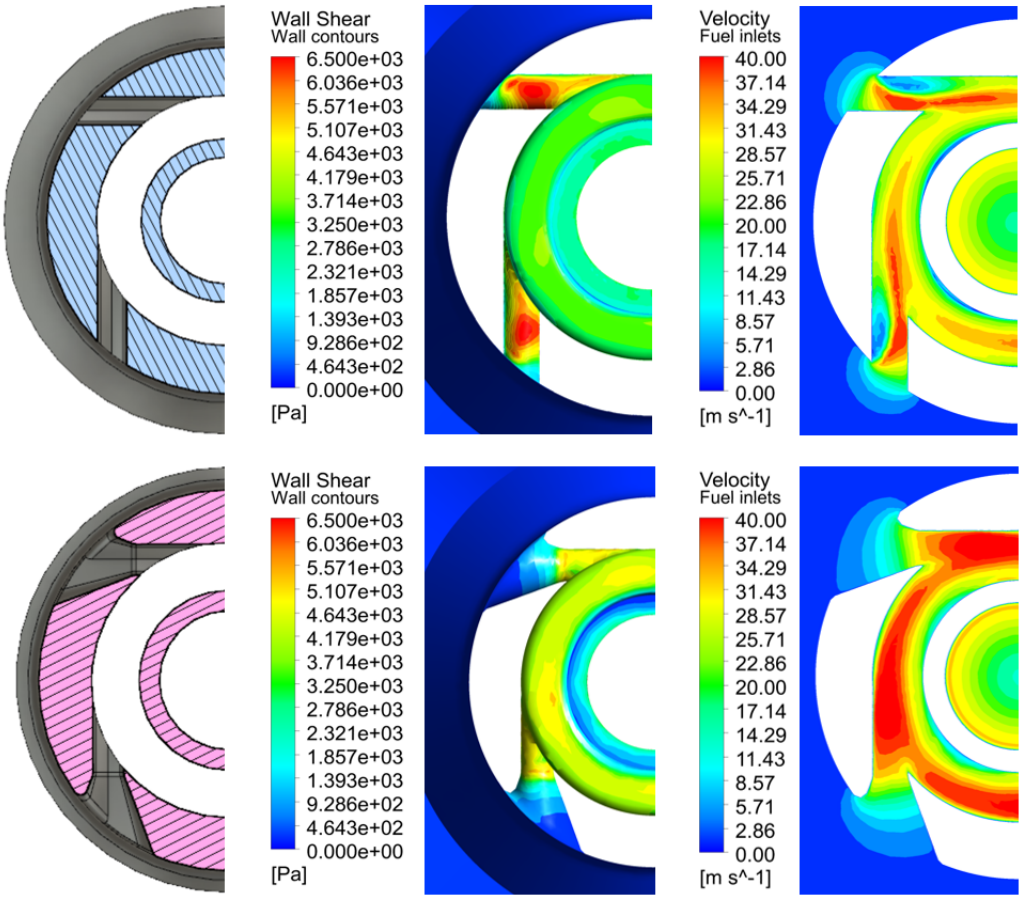

Figure 4.10: Tangential fuel inlet contours for the (*top*) baseline design and (*bottom*) modified design.

Although the max shear stress in the oxidizer nozzle is smaller in the modified design, there appears to be higher shear stresses downstream of the oxidizer nozzle and in the fuel annulus. This is attributed to the increased fluid momentum in these areas which will be discussed shortly. Most importantly, in Figure 4.10 there is shown to be no tangential inlet flow separation and the passage is flowing full ($\phi \sim 1$), thus eliminating the *vena contracta* effect.

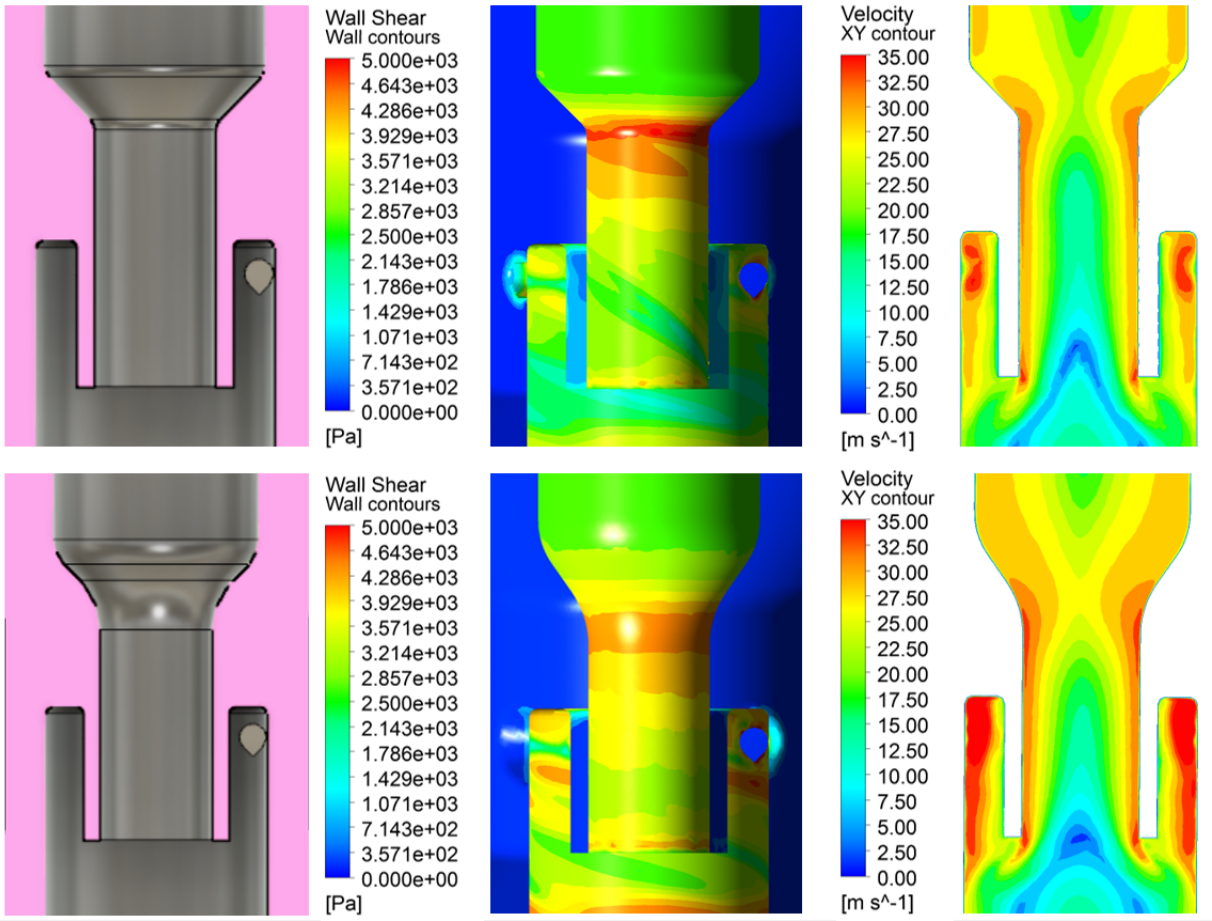

Figure 4.11: Oxidizer nozzle contours for the (*top*) baseline design and (*bottom*) modified design.

The change in discharge coefficient and net wall shear force between designs is reported in Table 4.3. There was a modest improvement to the oxidizer discharge coefficient and total shear force, but a significant improvement to the fuel discharge coefficient. Since the constriction of fuel inlets is greater than the oxidizer inlets, it follows that the tapering would

have a greater impact there. The modest improvement in the oxidizer discharge coefficient indicates that the tangential inlets are not the primary loss mechanism for the oxidizer stage, but instead may be due to the longer fluid path length. It has been reported previously that the large aspect ratio of swirl coaxial injectors is a primary contributor to the overall viscous loss of the injector [41]. Reducing the injector aspect ratio will be a focus of future designs.

Table 4.3: Quantitative hydraulic comparison between injector designs. Pressures and velocities are averaged in the fluid film at the injector outlet.

Injector	$C_{D,ox}$	$C_{D,f}$	**Net wall shear (lbf)**	$P_{tot}(bar)$	$V_z(m/s)$	$V_\theta(m/s)$
Baseline	0.370	0.068	0.74	1.67	13.21	11.60
Modified	0.400	0.081	0.70	2.29	16.07	13.36
Difference	8.1%	19.1%	-5.4%	33.6%	14.3%	18.4%

It was also of interest to examine how these design changes impacted the fluid momentum and total pressure at the outlet, which directly quantify the energy available for atomization and mixing. To examine these differences, the first task was to identify the liquid film thickness at the outlet and examine this region separately from the hollow gas core. As shown schematically in Figure 4.12, the film thickness was estimated by plotting the water volume fraction in the radial direction and finding the radial position that corresponded to a volume fraction cutoff limit of 95%. A distinct change in outlet behavior is shown in the film region on the right of Figure 4.12, confirming the location of the gas-liquid interface.

The liquid film thickness for the combined oxidizer and fuel streams was estimated to be approximately 0.012 inches by examination of the water volume fraction contour at the outlet. This combined stream film thickness is less than the individual film thicknesses reported in Table 2.1. This is most likely due to the difference in density and viscosity between water and actual propellants.

After isolating the liquid region at the outlet, the momentum and total pressure were compared between injector designs and averaged values are reported in Table 4.3. The relative changes shown in Figure 4.13 reveal significant increases. This will ultimately lead to a

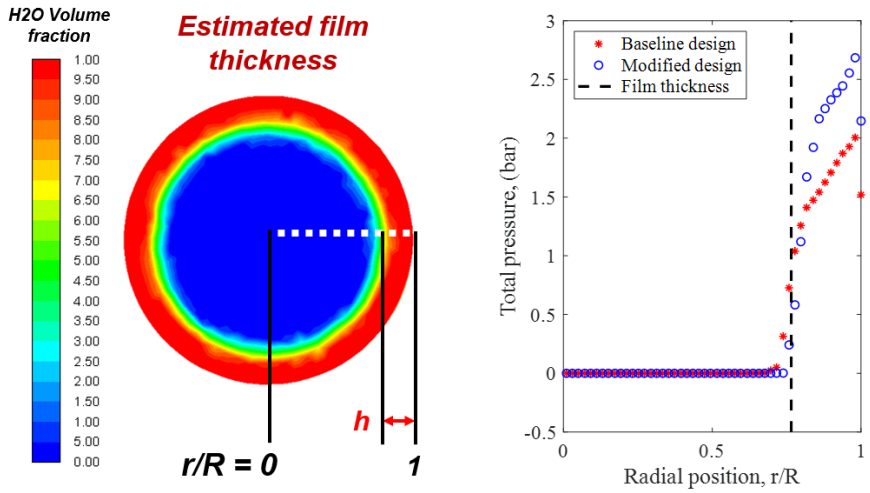

Figure 4.12: (*left*) Depiction of film thickness at injector outlet and (*right*) comparison of total pressure between injector designs. Radial positions to the left of the film thickness are the hollow gas core region, and to the right is the liquid film region.

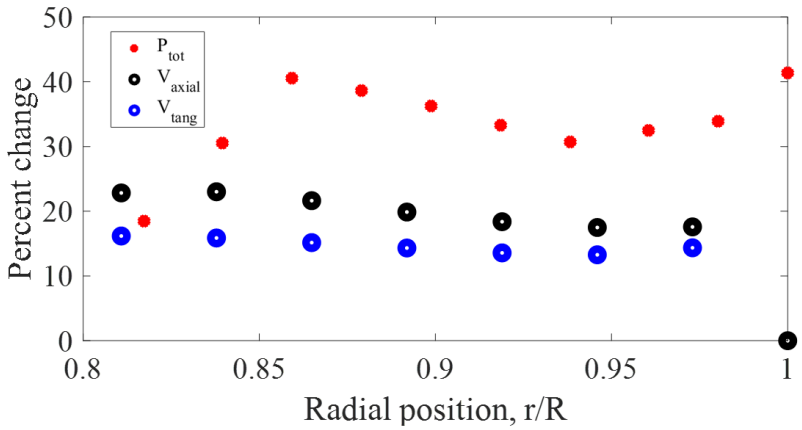

Figure 4.13: Relative changes in total pressure, axial velocity, and tangential velocity in the fluid film at the injector outlet.

shorter droplet breakup length, increased shearing between the propellants, and better mixing. Another interpretation is that since the injector is more hydraulically efficient, the same injection momentum can be achieved with a reduction in upstream pressure requirements, thus reducing tank and pump requirements. Ultimately, this leads to higher thrust-to-weight ratio propulsion systems and greater launch vehicle payload capacity.

CHAPTER 5

Conclusions and Future Directions

A canonical swirl coaxial injector for liquid rocket engines was modified for additive manufacturing and characterized with CFD modeling and cold-flow testing. The first important finding was that modification of the tangential inlets from a circular to a teardrop cross-sectional shape was found to have a relatively minor influence on C_D. Next, the analytical and computational C_D estimates for the baseline injector were found to agree well with each other and experimental results in literature, but differed from the cold-flow test results for the additively manufactured hardware. This quantified the added frictional losses that resulted from the inherently rougher surface finish. With these metrics obtained, surface roughness effects may be tuned in the CFD model to find a relative pipe roughness and compensated for during the design stage.

Potential actions to minimize the impact of increased surface roughness and realize the full benefit of AM include further design modifications and polishing of the printed hardware after manufacturing. Since the majority of the internal surfaces are unreachable to conventional polishing tools, techniques such as abrasive washing, or slurry honing, could be used. AM is still an evolving technology, with surface finish and dimensional accuracy expected to continue to improve with time, potentially negating these issues with minimal post-processing.

CFD results for the modified injector design enabled by AM highlighted reductions in both form and viscous losses. Specifically, fluid passageways were made less constrictive with tapering and fillets aimed at reducing wall shear stresses and eliminating flow separation. Compared to the baseline design, the modified injector has a predicted 19% increase in $C_{D,f}$,

an 8% increase in $C_{D,ox}$, and an 18% increase in angular momentum.

This work has demonstrated that AM is not only a tool for reducing manufacturing time and cost, but also for improving combustion device performance. To fully realize performance improvements, however, design optimization and post-manufacturing polishing techniques are important. Leveraging these recommendations and the design strategies presented in this work provides a pathway to more efficient combustion devices, and consequently, higher thrust-to-weight ratio propulsion systems and increased launch vehicle payload capacity. The role of AM is expected to continue to grow in the aerospace industry as well as others. As AM technology matures, increased capability and precision will grant engineers greater flexibility in inventing problem-solving technologies.

5.1 Hot-Fire Test Preparation

Future tasks include hot-fire testing both injectors to obtain actual combustion performance. The test goal will be to compare performance of the AM injectors at different recess ratios to one another, as well as to their conventionally manufactured counterparts. The plan is to obtain characteristic velocity (c^*) and pressure data in order to gain insight into performance and stability.

A combustor assembly has been designed and constructed to conduct this testing. This consists of an alloy steel combustion chamber, conical nozzle made of graphite, and composite ablative liner for thermal protection. A schematic of the assembly and the finished hardware is shown in Figure 5.1. In order to keep manufacturing simple and costs low, a 1-inch chamber diameter was used. All materials were standard stock sizes and the assembly was manufactured using a conventional mill and lathe. The steel chamber components were welded together.

The outstanding task to conduct testing is the development or acquisition of a liquid propellant test stand capable of handling cryogenic oxygen. This requires significant effort to develop from scratch and has been beyond the scope of this project. Fortunately, there

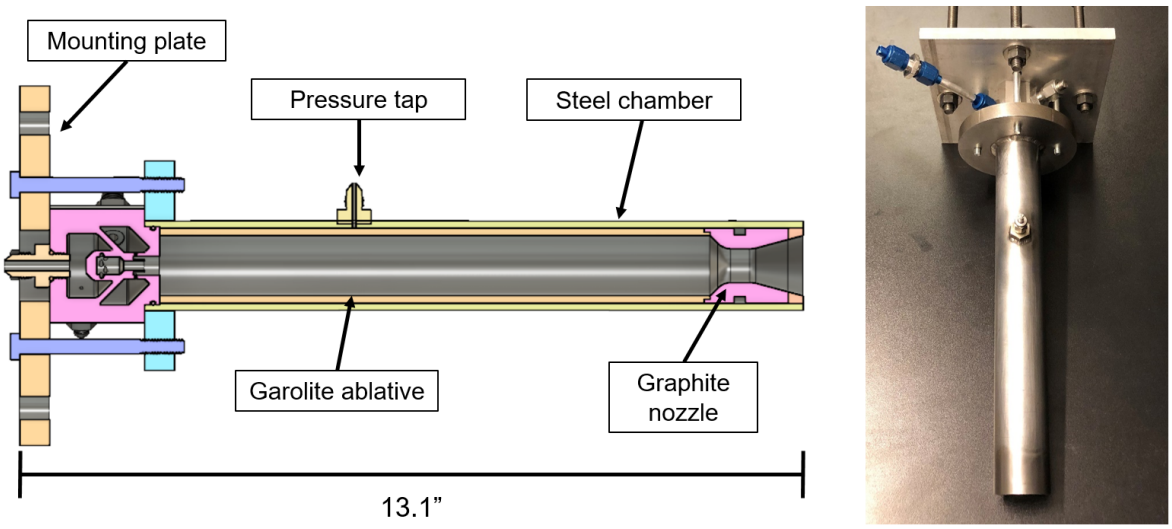

Figure 5.1: (*left*) Cross-sectional view of combustor assembly and (*right*) completed hardware assembly.

are two feasible paths forward. First, a low-thrust hybrid rocket motor test stand has recently been developed at UCLA with fluid, control, and instrumentation systems. It may be possible to modify this existing framework for LOx/Kerosene testing. Second, it is likely the Laser Spectroscopy and Gas Dynamics Laboratory will acquire a mobile rocket engine test stand in the near future which could also be used to test the injectors developed in this work.

5.2 Adapted Approach for Rotating Detonation Engines

The aerospace propulsion community has taken a significant interest in developing Rotating Detonations Engines (RDEs), both for air-breathing and rocket applications. RDEs offer numerous theoretical benefits over traditional propulsion systems. Conventional combustion utilizes deflagration, which is subsonic and an approximately constant pressure process described by the Brayton cycle. In contrast, RDEs leverage detonation waves, which are essentially chemically reacting shock waves that result in pressure gain. This is a nearly constant volume process described by the Humprey cycle. There are two immediate and

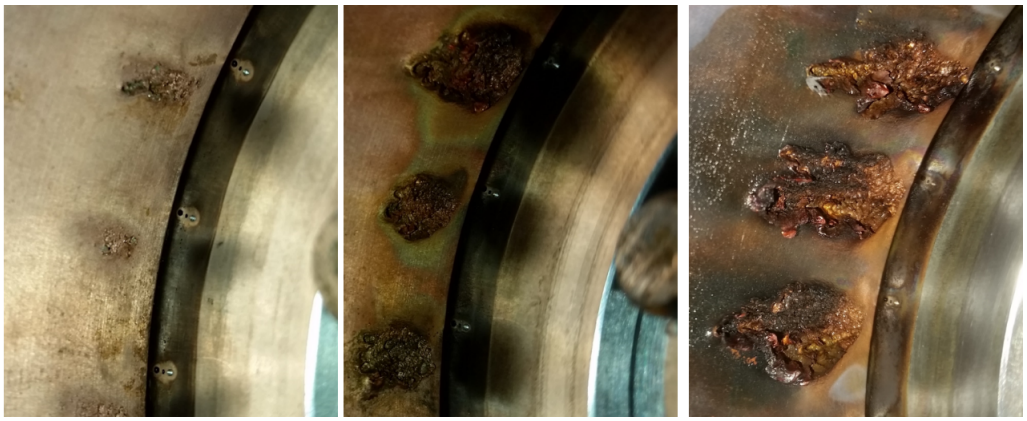

Figure 5.2: Thermal damage in RDE after 4, 8, and 12 hot-fire tests. Burn times lasted less than one second. Borrowed from [42].

important theoretical benefits of this. First, a pressure gain process can significantly reduce upstream feed systems such as pumps or compressors. This enables much higher chamber pressures to be achieved, which results in higher combustion efficiency via suppression of species dissociation and more complete combustion reactions. Second, the Humphrey cycle produces more work per cycle with lower entropy production in comparison to the Brayton cycle, resulting in increased thermal efficiency. Both of these factors can lead to systems with significantly higher thrust-to-weight ratios, enabling longer duration missions or increased vehicle payload capacity.

Unfortunately, there are several technological challenges currently preventing these theoretical performance gains from being realized. This is primarily due to the extremely harsh environment associated with detonations, which is highly transient with large thermal and pressure gradients. This causes three considerable issues: (1) undermixed propellants and relatively low wave speeds, (2) highly over-pressurized feed systems to prevent injector back flow, and (3) extreme heat fluxes and associated reduced hardware durability. All three of these issues are related to the propellant injector. An example of thermal damage in an RDE is shown in Figure 5.2.

Analysis-driven design coupled with AM can greatly enable improved injector designs that can theoretically address each of these issues. That is, AM can enable injector geometries that

can control forward and backward flow resistance, potentially decreasing upstream pressure requirements and reducing propellant refresh times scales. This would directly result in more time for the propellants to mix and approach the ideal chemical energy release. Unique AM geometries can also enable better thermal management by delivering fuel in boundary layer or film cooling schemes with significantly reduced manufacturing complexity.

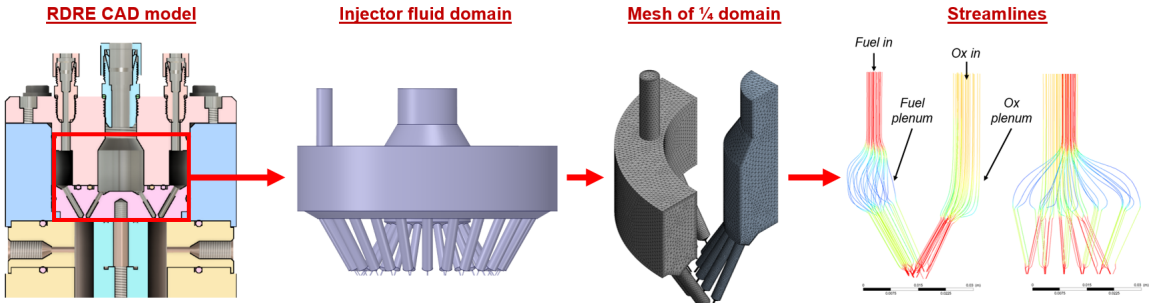

Figure 5.3: Impingement-style Rotating Detonation Rocket Engine (RDRE) injector with corresponding fluid modeling domain and example streamline results.

A similar CFD approach to this current work may be leveraged to analyze RDE injector hydraulics. However, due to the complex multi-physical interactions associated with detonation waves, more sophisticated models are needed for adequate design insight. This includes transient simulations to measure propellant refresh time, downstream atomization modeling to examine propellant mixing distribution, and coupled heat transfer simulations.

Initial RDE injector design and analysis work has begun. Current efforts aim to tune forward and backward flow resistance, as well as identify the best suited injector type for addressing the previously mentioned challenges. Thus far impinging and swirl coaxial injectors have been considered. An impinging RDE injector for MMH/NTO propellants was developed and tested by the Laser Spectroscopy and Gas Dynamics Laboratory in prior work. A preliminary modeling approach for this injector is shown in Figure 5.3. Impinging injectors have been successfully demonstrated in RDEs in numerous other studies as well. Advantages of this injector type include reasonable back flow resistance due to small orifice diameter ($\sim$ 0.015 in) and relatively high element density. Disadvantages include longer mixing time scales and poor thermal management. Swirl coaxial injector elements are also

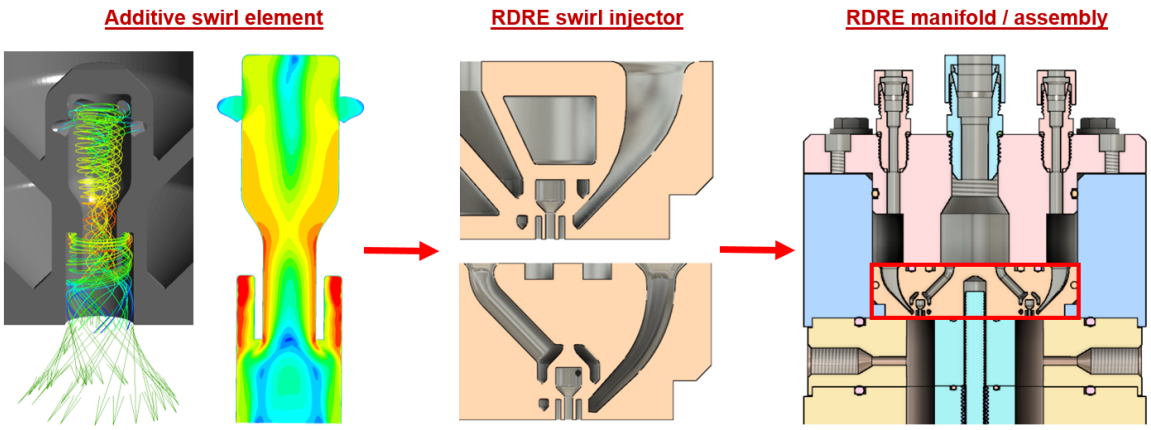

Figure 5.4: Swirl injector design concepts for RDRE.

being considered due to their enhanced mixing characteristics and ability to bias fuel near the walls for improved thermal management. Some notable limitations, however, include: (1) larger exposed orifice diameter and subsequent decrease in backward flow resistance, and (2) relatively lower element density at a given flowrate. The preliminary RDE swirl injector design approach is shown in Figure 5.4. The technical limitations of both injector types for RDE application motivates the use of unique AM-enabled geometries in order to achieve theoretical RDE performance.

References

[1] D. K. Huzel and D. H. Huang, *Modern Engineering for Design of Liquid-Propellant Rocket Engines*. American Institute of Aeronautics and Astronautics, 1992.

[2] V. Bazarov, V. Yang, and P. Puri, "Design and Dynamics of Jet and Swirl Injectors," in *Liquid Rocket Thrust Chambers*, Progress in Astronautics and Aeronautics, pp. 19–103, American Institute of Aeronautics and Astronautics, 1 2004.

[3] W. Anderson, M. Long, and S. Heister, "Liquid Bipropellant Injectors," in *Liquid Rocket Thrust Chambers*, Progress in Astronautics and Aeronautics, pp. 141–165, American Institute of Aeronautics and Astronautics, 1 2004.

[4] J. C. Najmon, S. Raeisi, and A. Tovar, *Review of additive manufacturing technologies and applications in the aerospace industry*. Elsevier Inc., 2019.

[5] Rocket Lab, "Electron Payload User Guide," no. 6.4, 2019.

[6] M. Wall, "Relativity Space will 3D-print rockets at new autonomous factory in Long Beach, California," *Space.com*, 2020.

[7] D. M. Atyam and N. H. Nguyen, "Designing and Testing Liquid Engines for Additive Manufacturing," in *51st AIAA/SAE/ASEE Joint Propulsion Conference*, AIAA Propulsion and Energy Forum, American Institute of Aeronautics and Astronautics, 7 2015.

[8] N. Patel, S. Standbridge, M. Van Den Berghe, and V. Devalaraju, "Design and additive manufacturing considerations for liquid rocket engine development," *AIAA Propulsion and Energy Forum and Exposition, 2019*, no. August, pp. 1–43, 2019.

[9] J. J. Hutt, *A Study of Design Details of Rocket Engine Swirl Injection Elements*. PhD thesis, Pennsylvania State University, 2001.

[10] G. S. Gill and W. H. Nurick, "Liquid Rocket Engine Injectors," tech. rep., 1976.

[11] Y. Vigor, M. Habiballah, J. Hulka, and M. Popp, *1.6.1 Coaxial Jet Injectors*. American Institute of Aeronautics and Astronautics, 2004.

[12] Space Exploration Technologies Corp, "Falcon User' s Guide," no. January, 2019.

[13] G. A. Dressier and J. M. Bauer, "TRW pintle engine heritage and performance characteristics," *36th AIAA/ASME/SAE/ASEE Joint Propulsion Conference and Exhibit*, no. July, 2000.

[14] P. Cheng, Q. Li, S. Xu, and Z. Kang, "On the prediction of spray angle of liquid-liquid pintle injectors," *Acta Astronautica*, vol. 138, no. March, pp. 145–151, 2017.

[15] P. R. Gradl, S. E. Greene, C. Protz, B. Bullard, J. Buzzell, C. Garcia, J. Wood, R. Osborne, J. Hulka, and K. G. Cooper, "Additive Manufacturing of Liquid Rocket Engine Combustion Devices: A Summary of Process Developments and Hot-Fire Testing Results," in *2018 Joint Propulsion Conference*, AIAA Propulsion and Energy Forum, American Institute of Aeronautics and Astronautics, 7 2018.

[16] C. DELBERT, "You Can Make a Rocket Engine's Entire Combustion Chamber in One 3D Print," 2019.

[17] D. Sher, "SpaceX's Crew Dragon spacecraft with 3D printed SuperDraco engines is now officially flying," 2019.

[18] H. Kawashima, T. Kobayashi, and K. Okita, "Progress of le-9 engine development," *2018 Joint Propulsion Conference*, no. Lmcc, pp. 1–10, 2018.

[19] M. W. Khaing, J. Y. Fuh, and L. Lu, "Direct metal laser sintering for rapid tooling: Processing and characterisation of EOS parts," *Journal of Materials Processing Technology*, vol. 113, no. 1-3, pp. 269–272, 2001.

[20] G. N. Abramovich, "Applied gasdynamics," *Moscow Izdatel Nauka*, 1976.

[21] Z. Kang, Z. g. Wang, Q. Li, and P. Cheng, "Review on pressure swirl injector in liquid rocket engine," *Acta Astronautica*, vol. 145, no. February, pp. 174–198, 2018.

[22] C. B. Greene, *Design and Experimentation of a Tangential Orifice Swirl Injector Using Liquid Oxygen and Gaseous Hydrogen*. PhD thesis, Pennsylvania State University, 2002.

[23] D. Kim, P. Han, J.-H. Im, Y. Yoon, and V. G. Bazarov, "Effect of Recess on the Spray Characteristics of Liquid-Liquid Swirl Coaxial Injectors," *Journal of Propulsion and Power*, vol. 23, pp. 1194–1203, 11 2007.

[24] S.-H. Kim, Y.-M. Han, S. Seo, I.-Y. Moon, J.-K. Kim, and W.-S. Seol, "Effects of LOx Post Recess on the Combustion Characteristics for Bi-Swirl Coaxial Injector," in *41st AIAA/ASME/SAE/ASEE Joint Propulsion Conference & Exhibit*, Joint Propulsion Conferences, American Institute of Aeronautics and Astronautics, 7 2005.

[25] K. Ahn, Y. M. Han, S. Seo, and H. S. Choi, "Effects of injector recess and chamber pressure on combustion characteristics of liquid-liquid swirl coaxial injectors," *Combustion Science and Technology*, vol. 183, no. 3, pp. 252–270, 2011.

[26] K. Ahn, Y. M. Han, and H. S. Choi, "Effects of recess length on discharge coefficients of swirl coaxial injectors," *Combustion Science and Technology*, vol. 184, no. 3, pp. 323–336, 2012.

[27] K. Ahn, J.-G. Kim, and H.-S. Choi, "Effects of injector recess on heat flux in a combustion chamber with cooling channels," *Aerospace Science and Technology*, vol. 37, pp. 110–116, 8 2014.

[28] X. Wang, Y. Wang, and V. Yang, "Geometric Effects on Liquid Oxygen/Kerosene Bi-Swirl Injector Flow Dynamics at Supercritical Conditions," *AIAA Journal*, vol. 55, no. 10, pp. 3467–3475, 2017.

[29] K. J. Lee, H. J. Kim, S. Seo, and H. S. Choi, "Experimental Verification for Acoustic Damping Enhancement by Gaps in Injector-Formed Baffles," *Journal of Propulsion and Power*, vol. 25, pp. 435–442, 3 2009.

[30] K.-J. Lee, S. Seo, J.-Y. Song, Y.-M. Han, H.-S. Choi, and W.-S. Seol, "Combustion Stability Assessment of Double Swirl Coaxial Injectors Using Simulant Propellants,"

in *41st AIAA/ASME/SAE/ASEE Joint Propulsion Conference & Exhibit*, no. July, pp. 1–9, 2005.

[31] K. Ahn and H.-S. Choi, "Combustion Dynamics of Swirl Coaxial Injectors in Fuel-Rich Combustion," *Journal of Propulsion and Power*, vol. 28, pp. 1359–1367, 11 2012.

[32] K. Ahn and H.-S. Choi, "An Extensive Study on the Discharge Coefficients of Open-Type Swirl Injectors," *Atomization and Sprays*, vol. 27, no. 10, 2017.

[33] "ANSYS FLUENT User's Guide, Release 20.1," tech. rep., 2020.

[34] M. Arienti, X. Li, M. Soteriou, C. Eckett, and R. Jensen, "Coupled Level-Set/Volume-of-Fluid Method for the Simulation of Liquid Atomization in Propulsion Device Injectors," in *46th AIAA/ASME/SAE/ASEE Joint Propulsion Conference & Exhibit*, no. July, pp. 1–10, 2014.

[35] G. Amini, "Liquid flow in a simplex swirl nozzle," *International Journal of Multiphase Flow*, vol. 79, pp. 225–235, 2016.

[36] "ANSYS FLUENT Theory Guide, Release 20.1," tech. rep., 2020.

[37] S. Acharya, B. R. Baliga, K. Karki, J. Y. Murthy, C. Prakash, and S. P. Vanka, "Pressure-based finite-volume methods in computational fluid dynamics," *Journal of Heat Transfer*, vol. 129, no. 4, pp. 407–424, 2007.

[38] W. Anderson and D. L. Bonhaus, "An implicit upwind algorithm for computing turbulent flows on unstructured grids," *Computers & Fluids*, vol. 23, no. 1, pp. 1–21, 1994.

[39] T.-H. Shih, W. W. Liou, A. Shabbir, Z. Yang, and J. Zhu, "A New K-epsilon Eddy Viscosity Model for High Reynolds Number Turbulent Flows: Model Development and Validation," no. August, 1994.

[40] D. M. Atyam and P. E. Sojka, "Characterization of Direct Metal Laser Sintered Impinging Injectors: Like-Doublet, Unlike Triplet, Unlike Quadlet, Unlike Pentad," in *53rd*

AIAA/SAE/ASEE Joint Propulsion Conference, AIAA Propulsion and Energy Forum, American Institute of Aeronautics and Astronautics, 7 2017.

[41] N. Zong and V. Yang, "Supercritical Fluid Dynamics of Pressure Swirl Injector with External Excitations," in *43rd AIAA/ASME/SAE/ASEE Joint Propulsion Conference & Exhibit*, no. July, 2012.

[42] W. Anderson, S. D. Heister, and C. Hartsfield, "Experimental Study of a Hypergolically Ignited Liquid Bipropellant Rotating Detonation Rocket Engine," in *AIAA Scitech 2019 Forum*, no. January, (Reston, Virginia), American Institute of Aeronautics and Astronautics, 1 2019.